Master thesis

Investigation of many-particle processes in Beryllium using the Multiconfigurational time-dependent Hartree-Fock method

by
Christopher Hinz

Kiel, 29 July 2013

Institut für
Theoretische Physik und Astrophysik
der Christian - Albrechts - Universität zu Kiel

Supervisor/1st examiner:	Prof. Dr. Michael Bonitz
2nd examiner:	Priv.-Doz. Dr. Dietmar Block

Abstract

In this work, we have investigated many-particle processes in beryllium using the Multiconfigurational time-dependent Hartree-Fock method (MCTDHF). This method allows us to gradually include correlations, i.e., contributions to the inter-particle interaction beyond a mean-field description. One process, in which are particularly interested, is the correlation-induced shake-up ionization. The eventual goal of this work is the time-resolved observation of these effects. To reach this goal, we introduce the many-particle quantum theory in the form of the first and second quantization. With these theories as a foundation, we will outline several numerical methods which can be used to numerically solve the time-dependent Schrödinger equation. On the basis of Configuration interaction and Hartree-Fock, we will motivate the Multiconfigurational time-dependent Hartree-Fock method (MCTDHF) and deduce it from first principles. To successfully solve the MCTDHF equations for a complex process such as photo-ionization of beryllium, we need to considerably speed up our implementation. First, we propose the Energy subspace projection (ESP) scheme to solve the issue of stiffness which prevents a proper time propagation of the MCTDHF equations. Afterwards, we introduce a parallelization scheme to enable the use of cluster computers as a means to accelerate the execution of the algorithm. After we have ensured that we can effectively perform the desired simulations, we explain the computer experiment and establish the necessary concepts. In the last part of this work, we will actually perform the outlined simulations and discuss our findings.

Zusammenfassung

In dieser Arbeit wurden Vielteilchenprozesse in Beryllium mittels der Multiconfigurational - time-dependent - Hartree-Fock - Methode untersucht. Diese Methode erlaubt es sukzessiv Korrelationen, das heißt Beiträge der Wechselwirkung zwischen zwei Teilchen jenseits einer Mean-field - Beschreibung, hinzuzufügen. Ein Prozess, für den wir uns insbesondere interessieren, ist der durch Korrelationen bedingte shake-up - Prozess. Das letztendliche Ziel dieser Arbeit ist die zeitaufgelöste Beobachtung dieser Effekte. Um dieses Ziel zu erreichen, werden wir eine Einführung in die Vielteilchenquantentheorie in Form der ersten und zweiten Quantisierung geben. Mit diesen Theorie als Grundlage, werden wir diverse numerische Methoden umreißen, welche dazu verwendet werden können dir zeitabhängige Schrödingergleichung zu lösen. Aufbauend auf Configuration interaction and Hartree-Fock werden wir die Multiconfigurational - time-dependent - Hartree-Fock - Methode (MCTDHF) motivieren und sie aus einem physikalischem Grundprinzip herleiten. Um die MCTDHF-Gleichungen erfolgreich für einen solch komplexen Prozess wie die Photoionization zu lösen, müssen wir unsere Implementierung deutliche beschleunigen. Als erstes schlagen wir das Energy-subspace-projection (ESP)-Schema vor, um das Problem der steifen Differentialgleichungen zu lösen, welches eine vernünftige Zeitentwicklung der MCTDHF-Gleichungen verhindert. Danach führen wir ein Parallelisierungsschema ein, um die Nutzung von Cluster-Computern als eine Möglichkeit zur Beschleunigung des Algorithmus zu ermöglichen. Nachdem wir sichergestellt haben, dass wir die gewünschten Berechnungen auch tatsächlich durchführen können, erklären wir das Computerexperiment und führen die benötigten Konzepte ein. Im letzten Teil dieser Arbeit werden wir die skizzierten Simulationen tatsächlich durchführen und unsere Befunde diskutieren.

Contents

1 Introduction

In the recent years, new light source, like LCLS at SLAC and Flash at DESY [1], with shorter and more powerful pulses have enabled the time-resolved observation of processes in atoms and molecules. Numerous techniques like streaking cameras [2] and the pump-probe scheme [3, 4] have been developed to capture the time-dependency of intra-atomic processes and have been successfully applied to atomic systems [5, 6]. Especially, complex many-particle processes like Auger decay have shown interesting behavior [7]. As a visionary goal, one hopes to manipulate the electronic structure of atoms in molecules in the future to allow for sophisticated technical applications by using the gained insights. Via the European XFEL, which is currently built in Hamburg and has recently reached a milestone of its construction, it is expected that new hurdles in this direction are overcome.

This sets a high standard for a theoretical description as the simulation of many-particle system is a non-trivial task. Traditional methods like Configuration interaction are not able to simulate more than two electrons at the same time [8, 9], which is in general insufficient to reach the same level of sophistication as the experiments do. Therefore, more elaborate methods have to be developed. In this work, we will use the Multiconfigurational time-dependent Hartree-Fock (MCTDHF) method, which allows to gradually include correlations in addition to the mean-field description of vanilla Hartree-Fock, to simulate many-particle processes in beryllium. Such many-particle processes are a good benchmark for any numerical method, as the correct description of these processes is a complex task. Recent calculation for the photo-ionization in Helium and Beryllium [10, 11] show promising results for MCTDHF. As the eventual goal, we will try to observe a many-particle process, like shake-up ionization and Auger decay, in a time-resolved manner by using the pump-probe scheme.

1.1 Overview

The present work is organized as follows:

- **Chapter 2** will lay the theoretical foundation for the numerical methods which are used in this work. In particular, we will introduce the first and second quantization.
- **Chapter 3** describes several methods to solve the time-dependent Schrödinger equation numerically. Most notably, we will motivate and deduce the Multiconfigurational time-dependent Hartree-Fock method which is the crucial point of this work.
- **Chapter 4** engages the issue of stiffness which inhibit the time propagation during the numerical solution of the MCTDHF equations. In this chapter, we will propose a domain-specific ansatz to circumvent this problem.
- **Chapter 5** introduces a parallelization scheme for the MCTDHF equations and presents its benefits and shortcomings.
- **Chapter 6** describes the computer experiment and introduces the necessary methods of measurement.
- **Chapter 7** discusses the numerical results which were obtained from the MCTDHF equations and presents our findings.
- **Chapter 8** summarizes this work and our conclusions. In addition, we give a brief outlook on possible future goals.

1.2 Remarks

In this work, we will use lower case bold letters $\boldsymbol{v}$ for vectors and upper case bold letters $\boldsymbol{A}$ for matrices and tensors. As usual in quantum theory, quantities $\hat{A}$ with a hat on the top denote linear operators.

Throughout this work, we will give all quantities in atomic units which is a unit system that is especially convenient for atomic physics. It is defined by the requirement

$$\hbar = e = m_e = \alpha \cdot c = 1. \tag{1.1}$$

This especially means that all distance are given in units of the Bohr radius, and all electric charges and masses in units of the electron charge and mass, respectively. The unit of energy in this unit system is named Hartree (Ha) which is defined as the potential energy of the hydrogen groundstate.

2 Theory of many-particle quantum mechanics

In this chapter we will lay the theoretical foundation for the numerical methods which are used in this work.

2.1 Mathematical structure of quantum theory

Before we will consider the details of many-particle quantum mechanics, we give a short review of the fundamental structure of quantum mechanics. Due to the focus of this work on atomic systems, we confine ourselves to a description in terms of so called pure states, which describes systems at temperature $T = 0$ K, instead of a more general description using an ensemble of states, that is necessary for systems at finite temperatures. This simplification is justified by the fact, that even in experimental setups each atom is separated from its environment as much as possible to avoid statistical noise. We will only give a brief and informal overview of the mathematical principles of quantum mechanics. A more rigorous introduction can be found, e.g., in [12] and [13].

The central structure of quantum mechanics is the state space, on which all operations are defined. From a mathematical point of view the quantum-mechanical state space is a Hilbert space $\mathcal{H}$, that is, a complete vector space equipped with a scalar product

$$\langle \cdot | \cdot \rangle : \mathcal{H} \times \mathcal{H} \to \mathbb{C}. \tag{2.1}$$

The elements of the state space are called state vectors, or states for short, and are usually denoted as $|x\rangle$, where x is an arbitrary label.

To formalize the relation between the scalar product (2.1) and the state vectors $|x\rangle$, it is useful to introduce the concept of the dual space. Any Hilbert space $\mathcal{H}$ has an associated dual space $\mathcal{H}^\dagger$, which is the space of all bounded linear functionals

$$\langle x | : \mathcal{H} \to \mathbb{C}. \tag{2.2}$$

The theory of dual spaces justifies the historical Bra-Ket notation, which was introduced by Paul Dirac in 1939 [14] and is ubiquitous in modern quantum theory. In this notation, one refers to the elements of $\mathcal{H}$ as ket states and to the elements

of $\mathcal{H}^\dagger$ as bra states. Using this formulation, we can adopt the definition

$$\langle x|y\rangle := \langle x|\,|y\rangle = \langle x|\,(|y\rangle) \tag{2.3}$$

of the scalar product (2.1). The advantage of this reformulation is that the right-hand side of (2.3) consists of mathematical objects on which we can apply mathematical rewriting rules, whereas the left-hand side is, individually, only a notation without inherent mathematical semantic. As stated by the Riesz representation theorem [15], the dual space $\mathcal{H}^\dagger$ is anti-isomorphic to the Hilbert space $\mathcal{H}$. This means in particularly that the mapping between bra states and ket states is unique, which we indicate by using the same label for associated states. If not stated otherwise below, we will only discuss the properties of the Hilbert space since almost all properties hold similarly for the dual space.

An important property, which every Hilbert space—as a complete vector space—possesses is that every state $|\psi\rangle$ can be represented as a superposition

$$|\psi\rangle = \sum_i \langle\phi_i|\psi\rangle\,|\phi_i\rangle \tag{2.4}$$

of arbitrary basis states $\{|\phi_i\rangle\}$. The expansion coefficients

$$c_i = \langle\phi_i|\psi\rangle \tag{2.5}$$

uniquely determine the state for a chosen basis set. In the following we will only discuss the theory for discrete basis sets, as the structure for continuous basis sets is primarily the same. Another frequently used property, which is tightly coupled to the expansion in basis states, is the expression of the identity operator $\hat{\mathbb{1}}\colon \mathcal{H} \to \mathcal{H}$ as

$$\hat{\mathbb{1}} = \sum_i |\phi_i\rangle\langle\phi_i|\,, \tag{2.6}$$

where $|\phi_i\rangle\langle\phi_i|$ denotes the outer product between the ket state $|\phi_i\rangle$ and its corresponding bra state $\langle\phi_i|$.

Another fundamental concept in quantum theory are linear operators $\hat{A} : \mathcal{H} \to \mathcal{H}$, which describe transformations on ket states. By analogy with the scalar product (2.3), one introduces the notation

$$\langle\Psi|\,\hat{A}\,|\Phi\rangle := \langle\Psi|\left(\hat{A}\,(|\Phi\rangle)\right). \tag{2.7}$$

For any linear operator $\hat{A}$ one can define —due to the correspondence of Hilbert space and dual space—its adjoint operator $\hat{A}^\dagger : \mathcal{H}^\dagger \to \mathcal{H}^\dagger$, which satisfies the identity

$$\langle\Psi|\,\hat{A}\,|\Phi\rangle = \left(\hat{A}^\dagger\,\langle\Psi|\right)|\Phi\rangle\,. \tag{2.8}$$

Again, we can use a basis $\{|\phi_i\rangle\}$ to represent the abstract operator $\hat{A}$ using

$$\hat{A} = \sum_{ij} \langle\phi_i| \hat{A} |\phi_j\rangle |\phi_i\rangle\langle\phi_j| , \tag{2.9}$$

As a corollary from equation (2.9), the structure of the operator only depends on the matrix elements

$$A_{ij} = \langle\phi_i| \hat{A} |\phi_j\rangle \tag{2.10}$$

for a given basis, which means that an operator is uniquely determined by its action on all basis states. This fact is usually exploited by substituting the abstract operator $\hat{A}$ with the matrix $\boldsymbol{A} = (A_{ij})$ after we have chosen a certain basis set. Together with the expansion, given by equation (2.4), this allows us to express all essential quantities in terms of a single basis set.

Physical quantities are represented by self-adjoint operators, which satisfy

$$\langle\phi_i| \hat{A} |\phi_J\rangle = \langle\phi_i| \hat{A} |\phi_J\rangle^\dagger \tag{2.11}$$

for every i and j. The arguably most important self-adjoint operator in quantum mechanics is the Hamilton operator, or Hamiltonian, which completely determines the properties of a physical system, much like the Hamilton function in classical mechanics. The quantum mechanical measurement of an observable is given by the expectation value of the associated self-adjoint operator. We will restrict ourself to projective measurements, which are usually used in standard quantum mechanics, as opposed to the more general positive-operator valued measure (POVM) [16]. In the case of projective measurements and pure states the expectation value of a self-adjoint operator $\hat{A}$ regarding a state $|\psi\rangle$ is defined by

$$\langle\hat{A}\rangle_{|\psi\rangle} = \langle\psi| \hat{A} |\psi\rangle . \tag{2.12}$$

Usually the considered state is fixed by convention and the subscript in equation (2.12) is omitted for brevity. If we use the identity (2.9) to substitute the operator in equation (2.12), we obtain

$$\langle\hat{A}\rangle_{|\psi\rangle} = \sum_{ij} A_{ij} \langle\psi|\phi_i\rangle \langle\phi_j|\psi\rangle . \tag{2.13}$$

The scalar products in equation (2.13) can be interpreted as expansion coefficients

$$c_i = \langle\phi_i|\psi\rangle \tag{2.14}$$

of the state $|\psi\rangle$ in the basis $\{|\phi_i\rangle\}$ and we finally arrive at a representation of the expectation value

$$\langle\hat{A}\rangle = \sum_{ij} A_{ij} c_i^* c_j \tag{2.15}$$

solely in terms of the chosen basis. Equation (2.15) can be simplified by choosing the eigenstates of operator $\hat{A}$, i.e., the states $\{|a_i\rangle\}$, which satisfy $\hat{A}\,|a_i\rangle = a_i\,|a_i\rangle$, as the basis. In this case the matrix $\boldsymbol{A}$ is diagonal with the values $\{a_i\}$ on the diagonal [1] and equation (2.15) rearranges into

$$\langle \hat{A} \rangle = \sum_i a_i c_i^* c_i = \sum_i a_i \left|c_i\right|^2 . \tag{2.16}$$

The expression

$$\left|c_i\right|^2 = \langle \psi | \, |\phi_i\rangle \langle \phi_i | \, |\psi\rangle \tag{2.17}$$

is the expectation value of the projector $|\phi_i\rangle\langle\phi_i|$ and can be interpreted as the probability that the state $|\phi_i\rangle$ is occupied. If we consider that the value a_i is the expectation value of the eigenstate $|a_i\rangle$ and that $\left|c_i\right|^2$ is the probability with which the state is occupied, one can interpret equation (2.16) as the weighted average of all possible measurement results.

For two operators, one defines the commutator

$$\left[\hat{A}, \hat{B}\right] = \hat{A}\hat{B} - \hat{B}\hat{A} \tag{2.18}$$

and the anti-commutator

$$\left\{\hat{A}, \hat{B}\right\} = \hat{A}\hat{B} + \hat{B}\hat{A}. \tag{2.19}$$

The commutator of two operators is a fundamental quantity, since it defines several important mathematical and physical properties of these operators, for example how Heisenberg's uncertainty principle applies to the quantities. Notably, if the commutator $\left[\hat{H}, \hat{A}\right]$ of the Hamiltonian and an arbitrary operator $\hat{A}$ is equal to zero, the quantity associated with the operator is conserved.

2.2 First quantization

In this section, we will introduce the so called first quantization, which describes the interaction of a quantum mechanical system with a classical environment, as a means to represent a many-particle system.

2.2.1 State space of many-particle quantum theory

After we have briefly reviewed the general mathematical formulation of quantum theory, we enlarge upon many-particle quantum theory. Based on a postulate of quantum theory [17], the state space of a composite system can be written

[1] This can be easily verified by applying the eigenstate property to the definition of the matrix elements.

as the tensor product of the state spaces associated with each component. If we only consider one kind of particles, for example electrons, and use the same single-particle Hilbert space $\mathcal{H}_1$ to describe each particle, the N-particle Hilbert space reads

$$\mathcal{H}_N = \bigotimes_{i=1}^{N} \mathcal{H}_1 = \mathcal{H}_1^{\otimes N}. \tag{2.20}$$

It should be noted, however, that there is no need to use the same single-particle Hilbert space for each particle, nor to use this decomposition at all. It is just the most commonly used one. As we will see later, it might not be the best idea to choose this representation in every situation.

While the state space $\mathcal{H}_N$ is sufficient to describe all N-particle systems, we need a more elaborate space in general, since we might add or remove particles from a state. The state space, which describes systems with an unspecified number of particles, is the Fock space

$$\mathcal{F} = \bigoplus_{N=0}^{\infty} \mathcal{H}_N. \tag{2.21}$$

While we need the Fock space for the formal description of many-particle theory, we will only describe systems with a fixed number of particles here. Therefore we will use $\mathcal{H}_N$ as the designated state space in most of this work. This is justified by the fact that the commutator $\left[\hat{H}, \hat{N}\right]$ between the Hamiltonian $\hat{H}$, which is used throughout this work, and the particle number operator $\hat{N}$ vanishes, i.e., the number of particles is a conserved quantity. Hence, we stay within the Hilbert space $\mathcal{H}_N$, if we start in a state $|\Psi\rangle \in \mathcal{H}_N$.

As a direct consequence of equation (2.20), the basis states of the N-particle Hilbert space can be represented as so called Hartree products

$$|\phi_1 \dots \phi_N) := |\phi_1\rangle \otimes |\phi_2\rangle \otimes \cdots \otimes |\phi_N\rangle\,, \tag{2.22}$$

where the $\{\phi_i\}$ denote the basis states of the single-particle Hilbert space $\mathcal{H}_1$. Using this representation, one can write an arbitrary N-particle state $|\Psi\rangle$ as

$$|\Psi\rangle = \sum_I C_I\, |\phi_1 \dots \phi_N) \tag{2.23}$$

using the already introduced basis expansion (compare Eq. (2.4)) with a multi-index $I = (i_1, i_2, \dots, i_N)$. The tensor product symbols within the Hartree product (2.22) are often omitted for brevity which results in the notation

$$|\phi_1\rangle\, |\phi_2\rangle \dots |\phi_N\rangle := |\phi_1\rangle \otimes |\phi_2\rangle \otimes \cdots \otimes |\phi_N\rangle\,. \tag{2.24}$$

2.2.2 Fermionic and bosonic Hilbert spaces

Due to an underlying principle of quantum theory, all particles of the same species—i.e., with identical intrinsic physical properties [2]—are indistinguishable, with quintessential consequences for the behavior and theory of quantum systems. This is contrasted by classical particles, which are always distinguishable. Through experiments, one has identified two families of particles with different behavior which are named fermions and bosons, respectively. The family of fermions encompasses all particle with half-integer spin—for example quarks, electrons and other leptons—while bosons are particles with integral spin—for example the Higgs boson, photons and certain composite systems. These findings are stated by the spin-statistics theorem [18, 19].

Let us now consider many-particle states, which consist of a single particle species, for example electrons with the same spin projection. The indistinguishably of these particles implies that such states must be essentially invariant under permutation of the single-particle states. Only the total phase of the state might change, since this does not affect its physical interpretation. As long as the Hamiltonian does not permit the decay of a fermion into one or more bosons and vice versa,

$$\left[\hat{H}, \hat{P}\right] = 0 \tag{2.25}$$

holds for every permutation operator $\hat{P} \in S_N$ on N-particles states. S_N is the symmetric group of N symbols. This is true for the Hamiltonians used in this work, since we only regard fermions in our models. Due to the vanishing commutator, the Hamiltonian and the permutation operators have common eigenstates, which form a basis of the N-particle Hilbert space $\mathcal{H}_N$ in this case. To obtain the eigenstates of all $\hat{P}$, one needs to solve the eigenvalue problem

$$\hat{P}\,|\nu\rangle = \nu\,|\nu\rangle \tag{2.26}$$

for each permutation operator. One finds that ν can only assume the value 1 or -1. The eigenspace which corresponds to the eigenvalue 1 is the subspace of totally symmetric functions $\mathcal{H}_N^+ \subset \mathcal{H}_N$ of bosonic states. In turn, the eigenspace, which is associated to the eigenvalue -1, is the subspace of totally antisymmetric functions $\mathcal{H}_N^- \subset \mathcal{H}_N$ and contains all fermionic states. Since $\left[\hat{H}, \hat{P}\right] = 0$ holds, any fermionic (bosonic) state will stay within $\mathcal{H}_N^-$ ($\mathcal{H}_N^+$), and it is sufficient to use the respective subspace as the state space. This significantly reduces the complexity of the theoretical description due to the reduced dimensionality with regard to the full N-particle Hilbert space H_N.

[2] This includes mass, electric charge, spin, etc.

To exploit this fact for fermionic systems and construct a basis of the subspace $\mathcal{H}_N^-$, it is convenient to define the projection operator $\hat{P}^-\colon \mathcal{H}_N \to \mathcal{H}_N^-$,

$$\hat{P}^- = \frac{1}{N!} \sum_{\hat{P} \in S_N} \operatorname{sign}(\hat{P})\, \hat{P}, \tag{2.27}$$

which can be applied to an arbitrary, non-symmetric state to obtain its anti-symmetric part. Here, the expression $\operatorname{sign}(\hat{P})$ denotes the parity of the permuation $\hat{P}$. Since $\hat{P}^-$ will generate non-normalized states, in general, one commonly defines the antisymmetrizer

$$\hat{\mathcal{A}} := \sqrt{N!}\hat{P}^- \tag{2.28}$$

to adjust the normalization. If one applies the antisymmetrizer to an arbitrary state

$$|\Psi\rangle = \sum_I C_I \,|\phi_1 \dots \phi_N)\,, \tag{2.29}$$

one can take advantage of the linearity of the antisymmetrizer and move it in front of the Hartree product. This results in the anti-symmetrized state

$$\left|\Psi^-\right\rangle = \sum_I C_I \hat{\mathcal{A}}\,|\phi_1 \dots \phi_N)\,. \tag{2.30}$$

This right-hand side of equation has already the structure of a basis expansion, if one chooses the states

$$|\phi_{i_1}\phi_{i_2}\dots\phi_{i_N}\rangle := \hat{\mathcal{A}}\,|\phi_1 \dots \phi_N) \tag{2.31}$$

as the basis states of $\mathcal{H}_N^-$. The $\{|\phi_{i_1}\phi_{i_2}\dots\phi_{i_N}\rangle\}$ are called (Slater) determinants, since one can write them equally as

$$|\phi_{i_1}\phi_{i_2}\dots\phi_{i_N}\rangle = \frac{1}{\sqrt{N!}} \begin{vmatrix} |\phi_1\rangle & |\phi_1\rangle & \dots & |\phi_1\rangle \\ |\phi_2\rangle & |\phi_2\rangle & \dots & |\phi_2\rangle \\ \vdots & \vdots & \ddots & \vdots \\ |\phi_N\rangle & |\phi_N\rangle & \dots & |\phi_N\rangle \end{vmatrix}. \tag{2.32}$$

Analogously, one can define a projector $\hat{P}^+\colon \mathcal{H}_N \to \mathcal{H}_N^+$,

$$\hat{P}^+ = \frac{1}{N!} \sum_{\hat{P} \in S_N} \hat{P}, \tag{2.33}$$

onto the subspace of fully symmetric functions and a symmetrizer

$$\hat{\mathcal{S}} := \sqrt{\frac{N!}{n_1!n_2!\dots n_{N_b}!}}\hat{P}^+, \tag{2.34}$$

where n_i indicates, how many particles occupy the i-th single-particle basis state. N_b labels the total number single-particle basis states. If we apply the symmetrizer to a Hartree product, one obtains what is called a permanent.

Another typically used representation of determinants and permanents is the so called occupation number representation

$$|n_1 n_2 \dots n_{N_b}\rangle\,, \tag{2.35}$$

The single-particle states are normally denoted as orbitals or modes in this case.

Usually our system will not solely consist of a single particle species. For example, atomic systems generally contain electrons with spin-up and spin-down. As these two species are distinguishable, we cannot use Slater determinants to represent the states. Instead, the Hilbert space $\mathcal{H}_N$ can be decomposed into a Hilbert space $\mathcal{H}^{\uparrow}_{N_\alpha}$ for the spin-up electrons and another Hilbert space $\mathcal{H}^{\downarrow}_{N_\beta}$ for the spin-down electrons, such that

$$\mathcal{H}_N = \mathcal{H}^{\uparrow}_{N_\alpha} \otimes \mathcal{H}^{\downarrow}_{N_\beta} \tag{2.36}$$

holds. Since $\mathcal{H}^{\uparrow}_{N_\alpha}$ as well as $\mathcal{H}^{\downarrow}_{N_\beta}$ are entirely associated to a single particle species, one can use Slater determinants as a basis for each Hilbert space once more. Due to the product structure of the N-particle Hilbert space $\mathcal{H}_N$, its basis states can be written as tensor products

$$\left|n_1 n_2 \dots n_{N_b}\right\rangle = \left|n_1 n_2 \dots n_{N_b^\alpha}\right\rangle \otimes \left|n_1 n_2 \dots n_{N_b^\beta}\right\rangle \tag{2.37}$$

of the spin-up $\left|n_1 n_2 \dots n_{N_b^\alpha}\right\rangle$ and spin-down Slater determinants $\left|n_1 n_2 \dots n_{N_b^\beta}\right\rangle$. N_b^α and N_b^β are the number of spin-up and spin-down orbitals, respectively, for which $N_b = N_b^\alpha + N_b^\beta$ is valid. One can construct arbitrarily complex Hilbert spaces in this manner by recursively decomposing the Hilbert space until each of the component spaces is associated with a single particle species.

2.2.3 The many-particle Hamiltonian

Before we will continue to establish the many-particle quantum theory, we will introduce the many-particle Hamiltonian,

$$\hat{H} := \sum_i \hat{h}_i + \frac{1}{2}\sum_{i\neq j} \hat{g}_{ij}, \tag{2.38}$$

that is used throughout this work.

$\hat{h}_i$ denotes the single-particle Hamiltonian, which acts on the i-th orbital, and can be written as

$$\hat{h}_i := \frac{\hat{\boldsymbol{p}}_i^2}{2} + V(\hat{\boldsymbol{r}}_i) + V_{\mathrm{EM}}(\hat{\boldsymbol{r}}_i, t) \tag{2.39}$$

in our case. The first term of the Hamiltonian (2.39) corresponds to the kinetic energy of the particle, while the second term provides the time-independent part of the potential energy. In the case of atomic systems

$$V(\hat{\boldsymbol{r}}_i) := \frac{-Z}{\hat{\boldsymbol{r}}_i} \tag{2.40}$$

is the Coulomb potential of the atomic core. The last term, $V_{\mathrm{EM}}(\hat{\boldsymbol{r}}_i, t)$, represents the classical electron-magnetic field, which is used to excite the system. In this work, we use the dipole approximation,

$$V_{\mathrm{EM}}(\hat{\boldsymbol{r}}_i, t) := \boldsymbol{E}(t)\hat{\boldsymbol{r}}_i, \tag{2.41}$$

in length gauge with an electric field $\boldsymbol{E}(t)$. This approximation neglects the spatial dependency of the field, and is therefore only valid if the wavelength of the field is large in comparison to the extent of the system.

The second term of the many-particle Hamiltonian (2.38) expresses the inter-particle interaction. For electrons, the interaction operator,

$$\hat{g}_{ij} := \frac{1}{|\hat{\boldsymbol{r}}_i - \hat{\boldsymbol{r}}_j|} \tag{2.42}$$

depicts the Coulomb interaction between two particles. While we will keep this choice during this work, other interactions, for example contact interaction, are imaginable.

2.3 Second quantization

After we have familiarized ourself with the theoretical description of many-particles in the so called first quantization, we will now introduce the second quantization, which is based on the occupation number representation and simplifies the description of arbitrary many-particle systems by formalizing the creation and structure of many-particle states. This is done by defining the so called annihilation and creation operators. We will restrict ourself to the case of fermions, since we will just use this case in this work. A nice property of the second quantization is that the structure for bosons is almost equal to the fermionic case, so one can transfer the obtained insights easily.

2.3.1 Annihilation and creation operators

As mentioned above, the main building block of the second quantization theory are the annihilation and creation operators, which formalize the destruction and

creation of a particle in a specific orbital. For an arbitrary state $|n_1 n_2 \dots n_{N_b}\rangle$ the action of the creation operator is defined by

$$\hat{a}_i^\dagger \, |n_1 n_2 \dots n_{N_b}\rangle = \delta_{n_i,0} \Gamma_i^{\boldsymbol{n}} \, |n_1 n_2 \dots n_i = 1 \dots n_{N_b}\rangle \,, \tag{2.43}$$

where the factor $\Gamma_i^{\boldsymbol{n}}$ specified as

$$\Gamma_i^{\boldsymbol{n}} := \prod_{j=1}^{i-1} (-1)^{n_j} \,. \tag{2.44}$$

Likewise, one defines the action of the annihilation operator as

$$\hat{a}_i \, |n_1 n_2 \dots n_{N_b}\rangle = \delta_{n_i,1} \Gamma_i^{\boldsymbol{n}} \, |n_1 n_2 \dots n_i = 0 \dots n_{N_b}\rangle \,. \tag{2.45}$$

The factor $\delta_{n_i,0}$ in equation (2.43) is necessary to satisfy the Pauli exclusion principle, thus, the quantum mechanical principle that no two fermions may occupy the same quantum state simultaneously. If this happens, the entire state is destroyed and we obtain the unphysical state 0. Similarly, one can not destroy a non-existing particle and the factor $\delta_{n_i,1}$ ensures, that the state is invalidated in this case. The creation operators $\hat{a}_i^\dagger$ and the annihilation operators $\hat{a}_j$ are connected by the identity

$$\hat{a}_i^\dagger = (\hat{a}_i)^\dagger \,. \tag{2.46}$$

In summary, these operators give us the ability to move through different subspaces of the Fock space, on which these operators are defined.

With the ability to create and destroy particles in certain orbitals at will, one can now systematically construct any desired many-particle state. If $|\text{vac}\rangle$ names the vacuum state, i.e., the unique state of a system with zero particles, one can write an arbitrary determinant $|\boldsymbol{n}\rangle = |n_1 n_2 \dots n_{N_b}\rangle$ as

$$|\boldsymbol{n}\rangle = \prod_{i=1}^{N_b}{}' \left(\hat{a}_i^\dagger\right)^{n_i} |\text{vac}\rangle \,. \tag{2.47}$$

It should be noted that the product in equation (2.47) should be interpreted as an ordered product, which can be surprising, if one is used to the behavior of products for real numbers. This is necessary, since the multiplication of creation operators is not commutative in general. Two different multiplication orders will always result in determinants, which have the same occupation, but might differ by a factor (-1). It is therefore important to choose a specific order and to restore the order while keeping track of the sign changes, if one adds another creator upfront. This is the reason for the factor $\Gamma_i^{\boldsymbol{n}}$ in the equations (2.43) and (2.45). The relation

between the creation and annihilation operators can be mathematically expressed by the anti-commutator relations

$$\left\{\hat{a}_i^\dagger, \hat{a}_j\right\} = \delta_{ij} \tag{2.48}$$

and

$$\left\{\hat{a}_i^\dagger, \hat{a}_j^\dagger\right\} = \left\{\hat{a}_i, \hat{a}_j\right\} = 0. \tag{2.49}$$

This simple and strictly formalized framework is the major strength of the second quantization and has lead to the broad adoption of this technique within the many-particle quantum theory community. Virtually the same formalism can be applied to bosonic systems or systems with a mixture of particle species, up to arbitrarily complex systems, without designing a new theory for every system from scratch. In fact, systems where the number of particles of a certain species—or even the total number of particles—is not fixed are treatable using this approach. For example one only has to substitute the anti-commutators with commutators and discard the Pauli principle to use the same methods for bosons.

2.3.2 Reduced density matrices and observables

To conclude the section about the second quantization, we will examine how one can represent operators, matrix elements and expectation values within the second quantization framework.

One can show that a many-particle operator $\hat{A}$ with one-particle characteristic can be expressed [13] as

$$\hat{A} = \sum_{ij} a_{ij} \hat{a}_i^\dagger \hat{a}_j \tag{2.50}$$

using the matrix elements

$$a_{ij} := \langle i | \, \hat{a} \, | j \rangle \tag{2.51}$$

and the creation $\hat{a}_i^\dagger$ and annihilation operators $\hat{a}_j$. $\langle i|$ and $|j\rangle$ are abbreviations for the basis states $\langle \phi_i|$ or $|\phi_j\rangle$. Similarly, one can express a many-particle operator $\hat{G}$ with two-particle characteristic as

$$\hat{G} = \sum_{ijkl} g_{ijkl} \hat{a}_i^\dagger \hat{a}_k^\dagger \hat{a}_l \hat{a}_j \tag{2.52}$$

with tensor elements

$$g_{ijkl} := \langle i | \, \langle k | \, \hat{g} \, | l \rangle \, | j \rangle \, . \tag{2.53}$$

After comparing equations (2.50) and (2.52), one would expect that all operators have the same structure within the second quantization. This is indeed true and

makes it straight forward to generalize the representation to arbitrary n-particle operators.

By inserting the second quantization representation of one- and two-particle operators (2.50) and (2.52) into the definition of the expectation value (2.12), we obtain the expressions

$$\langle \hat{A} \rangle = \sum_{ij} a_{ij} D_{ij} \tag{2.54}$$

and

$$\langle \hat{G} \rangle = \sum_{ijkl} g_{ijkl} d_{ijkl} \tag{2.55}$$

for the one- and two-particle expectation values.

$$D_{ij} := \langle \Psi | \, \hat{a}_i^\dagger \hat{a}_j \, | \Psi \rangle \tag{2.56}$$

and

$$d_{ijkl} := \langle \Psi | \, \hat{a}_i^\dagger \hat{a}_k^\dagger \hat{a}_l \hat{a}_j \, | \Psi \rangle \tag{2.57}$$

denote the one- and two-particle reduced density matrix, respectively. They can be easily calculated with the aid of the anti-commutator relations (2.48) and (2.49). Similarly, we can calculate matrix elements of these operators, which leads, for example, to the expression

$$\langle I | \, \hat{A} \, | J \rangle := \sum_{ij} a_{ij} \, \langle I | \, \hat{a}_i^\dagger \hat{a}_j \, | J \rangle \tag{2.58}$$

for an operator with one-particle characteristic.

Furthermore, also the structure of the operators itself gives us a significant advantage. Neither the values of the matrix elements nor the formal representation of the operator depend on the structure of the many-particle system, since these characteristics are exclusively covered by the annihilation and creation operators. As a result, one can reuse the already calculated matrix elements for many-particle systems with another structure instead of calculating them anew every time. The Hamiltonian, which is used throughout this work, reads

$$\hat{H} = \sum_{pq} h_{pq}(t) \, \hat{a}_p^\dagger \hat{a}_q + \frac{1}{2} \sum_{pqrs} g_{pqrs} \, \hat{a}_p^\dagger \hat{a}_r^\dagger \hat{a}_s \hat{a}_q \tag{2.59}$$

in the second quantization representation. Here, the

$$\{ h_{pq}(t) \} := \langle \phi_p | \, \hat{h} \, | \phi_q \rangle \tag{2.60}$$

and the

$$\{ g_{pqrs} \} := \langle \phi_p | \, \langle \phi_r | \, \hat{g} \, | \phi_s \rangle \, | \phi_q \rangle \tag{2.61}$$

denote the matrix elements of the single-particle Hamiltonian and the two-electron interaction, respectively.

3 Numerical methods

In this chapter, we introduce the Multiconfigurational time-dependent Hartree-Fock method (MCTDHF), which is used to carry out all numerical simulations in this work. As a first step, we briefly introduce two other methods—the Configuration interaction and the Hartree-Fock method—, which precede the MCTDHF method, and discuss their advantages and shortcomings. Afterwards, we develop the idea of MCTDHF, starting from the previously discussed methods and derive the corresponding equation of motion from first principles. As a conclusion of this chapter, we discuss several aspects of our implementation, e.g., the choice of the single-particle basis.

3.1 Configuration interaction

The main goal of this chapter is to enable us to numerically solve the time-dependent Schrödinger equation (TDSE),

$$\mathrm{i}\frac{\partial}{\partial t}\left|\Psi\right\rangle = \hat{H}\left|\Psi\right\rangle, \tag{3.1}$$

for a many-particle system which is described by an arbitrary many-particle Hamiltonian $\hat{H}$. One way which is theoretically straight forward is to discretize the TDSE using the principles introduced in chapter 2. We make the basis expansion ansatz

$$\left|\Psi\right\rangle = \sum_J C_J(t)\left|J\right\rangle \tag{3.2}$$

for the many-particle state. Up to now, the $\{|J\rangle\}$ are unspecified time-independent many-particle basis states, which are called configurations in this treatment. Since the state is time-dependent, we also have to use time-dependent expansion coefficients. For the sake of convenience, we will assume that the basis states are orthonormal, i.e.,

$$\left\langle I|J\right\rangle = \delta_{I,J} \tag{3.3}$$

holds for each I and J. In principle, one could derive the equations for non-orthonormal basis states, but from a practical point of view the added complexity is almost never worth the effort We will presume orthonormal many-particle states below if not stated otherwise. This implies that the orbitals are also orthonormal.

After inserting the expansion into the TDSE and multiplying it with a bra state $\langle I|$ from the left, one obtains the equation

$$\sum_J \mathrm{i}\frac{\partial}{\partial t} C_J(t) \langle I|J\rangle = \sum_J \langle I| \hat{H} |J\rangle C_J. \tag{3.4}$$

During the transformation of equation (3.4), we have utilized the interchangeability of the time derivative and the bra state, since it is time-independent, the linearity of all operators. To express the TDSE in a discretized fashion, which is numerically tractable, we define the Hamilton matrix

$$H_{IJ} := \langle I| \hat{H} |J\rangle \tag{3.5}$$

and exploit the previously required orthonormality to simplify the left-hand side. In doing so, we arrive at the discretized TDSE in coefficient notation,

$$\mathrm{i}\frac{\partial}{\partial t} C_J(t) = \sum_J H_{IJ} C_J, \tag{3.6}$$

or in vector notation,

$$\mathrm{i}\frac{\partial}{\partial t} \boldsymbol{C}(t) = \boldsymbol{H}\boldsymbol{C}. \tag{3.7}$$

The last step is to calculate the elements of the Hamilton matrix $\boldsymbol{H}$. Before we do this, we inspect how we can include the spin into our considerations. In this work, we will restrict ourselves to the spin-restricted treatment, that is the choice

$$|\phi_i^\alpha\rangle := |\phi_i\rangle |\uparrow\rangle , \tag{3.8}$$

$$\left|\phi_i^\beta\right\rangle := |\phi_i\rangle |\downarrow\rangle \tag{3.9}$$

for the spin orbitals. In contrast to the spin-unrestricted ansatz, which uses different spatial orbitals for each spin projection, the spin-restricted ansatz uses the same spatial orbital $|\phi_i\rangle$ to construct the corresponding spin orbitals $\left|\phi_i^{\alpha/\beta}\right\rangle$ for each spin projection. This ansatz works well, as long as the behavior of the particles in the same orbital does not depend on their spin projection. This is fulfilled for example in the case of our standard Hamiltonian (2.59) and Beryllium. A detailed discussion of all possible treatments for the spin can be found in [20].

Since the spin-up and spin-down particles are distinguishable, we use the ansatz

$$|K = (I, J)\rangle = |I\rangle |J\rangle \tag{3.10}$$

for the many-particle basis states, according to the discussion at the end of section 2.2.2. Here, $|I\rangle$ and $|J\rangle$ denote the Slater determinants, which are constructed from the spin-up orbitals and the spin-down orbitals, respectively.

The only difference in the many-particle Hamiltonian (2.59), if we incorporate the spin using the spin-restricted ansatz, are additional spin indices for the annihilation and creation operators. The matrix elements do not receive additional indices, since they are independent of the spin projection. Mathematically speaking, they are diagonal with respect to the spin indices. Thus, we arrive at the Hamiltonian

$$\hat{H} = \sum_{pq\sigma} h_{pq}(t)\, \hat{a}^\dagger_{p\sigma}\hat{a}_{q\sigma} + \frac{1}{2}\sum_{pqrs\sigma\tau} g_{pqrs}\, \hat{a}^\dagger_{p\sigma}\hat{a}^\dagger_{r\tau}\hat{a}_{s\tau}\hat{a}_{q\sigma}. \tag{3.11}$$

Since the matrix elements do not depend on the spin indices, it is useful to define the single and double excitation operators

$$\hat{E}_{pq} := \sum_{\sigma} \hat{a}^\dagger_{p\sigma}\hat{a}_{q\sigma} \tag{3.12}$$

$$\hat{e}_{pqrs} := \sum_{\sigma\tau} \hat{a}^\dagger_{p\sigma}\hat{a}^\dagger_{r\tau}\hat{a}_{s\tau}\hat{a}_{q\sigma} \tag{3.13}$$

with which we can reduce equation (3.11) to the form

$$\hat{H} = \sum_{pq} h_{pq}(t)\, \hat{E}_{pq} + \frac{1}{2}\sum_{pqrs} g_{pqrs}\, \hat{e}_{pqrs}. \tag{3.14}$$

The formal calculation of the Hamiltonian matrix elements is now straight forward, we only need to exploit the linearity of the operators to arrive at

$$\begin{aligned} H_{KL} &:= \langle K|\, \hat{H}\, |L\rangle = \\ &= \sum_{pq} h_{pq}(t)\, \langle K|\, \hat{E}_{pq}\, |L\rangle + \frac{1}{2}\sum_{pqrs} g_{pqrs}\, \langle K|\, \hat{e}_{pqrs}\, |L\rangle\,. \end{aligned} \tag{3.15}$$

The matrix elements of the excitation operators can systematically be calculated as detailed in section 2.3.2, by exploiting that the creation and annihilation operators only operate on either the spin-up determinant in ansatz (3.10) or the spin-down determinant.

As of now, we could integrate the CI equations with the major advantage that we would obtain an exact solution of the TDSE, safe for numerical errors from the truncation of the single-particle basis. The major downside of this treatment is that we have to use a set of $\binom{N_b}{N_\alpha}\binom{N_b}{N_\beta}$ Slater determinants for our calculations, which are far too many basis functions for realistic calculations, if we use more than two particles.

3.2 Hartree-Fock

To circumvent the drawbacks of the CI ansatz, we can exploit that it is often not necessary to calculate the exact solution to obtain a proper description of the physical system. Therefore, we can often use a scheme which gives a sufficiently good approximation of the exact solution. In this case we do not need to describe the entire Hilbert space to obtain the state, but can hope to find a well selected subspace in which the state resides approximately at every time point. Since the proper subspace might vary over time we can not use fixed orbitals to represent our state. Instead, the Hartree-Fock ansatz uses time-dependent orbitals—the Hartree-Fock orbitals—to build a single Slater determinant. Due to the restriction to a single determinant, one only needs $M = N_\alpha = N_\beta$ orbitals for the spin-restricted ansatz. The time-dependent orbitals themselves are represented using the ansatz

$$|\phi_n(t)\rangle = \sum_{j=1}^{N_b} b_{nj}(t)\,|\psi_j\rangle \tag{3.16}$$

using a time-independent basis set $\{|\psi_j\rangle\}$ with dimensionality N_b and time-dependent expansion coefficients $\{b_{nj}(t)\}$. The Hartree-Fock equations determine a set of, in some sense, optimal expansion coefficients to span the required subspace at every time-point. We will not deduce the equations at this point, as they are later later included in the MCTDHF equations as a special case.

The major advantage of this ansatz is that it is very cheap, since we only need to determine M coefficients, where M is usually small for our systems, because we only want to describe systems with a comparably small number of particles. The major disadvantage of the method is that it only covers the mean-field interaction between the particles i.e., only the interaction of a particle with the additional background potential—created by all other particles—is included, while the feedback of its movements onto other particles—and therefore their fields—is not. These contributions beyond the mean-field are called correlations. Since we are explicitly interested in many-particle processes, which are caused by correlations, Hartree-Fock is not sufficient to cover our needs.

3.3 Multiconfigurational time-dependent Hartree-Fock

In this section, we will introduce the Multiconfigurational time-dependent Hartree-Fock (MCTDHF) method as a hybrid scheme which combines CI and Hartree-Fock. After we have presented the general idea, we will deduce the equations of motion and will close with a discussion of our implementation.

3.3.1 Idea

While the Hartree-Fock ansatz is not sufficient to describe our systems, its benefits are too promising to be simply dismissed. One might get the idea that it may be favorable to combine the ideas of CI and Hartee-Fock to eliminate their disadvantages, while hopefully retaining most of their advantages. This was first proposed by Cederbaum et. al [21] in 2007 in the form of the MCTDH method which describes systems without exchange interaction. While this restriction does not hold for our systems, the generalization of this idea is direct and straightforward.

It leads to the MCTDHF ansatz

$$|\Psi\rangle = \sum_{\boldsymbol{n}} C_{\boldsymbol{n}}(t)\,|\boldsymbol{n};t\rangle\,, \tag{3.17}$$

which uses several time-dependent configurations to represent the many-particle state, instead of only one. Just like in Hartree-Fock, the time-dependent configurations are build from M time-dependent orbitals

$$|\phi_n(t)\rangle = \sum_{j=1}^{N_b} b_{nj}(t)\,|\psi_j\rangle\,, \tag{3.18}$$

which are itself represented by means of a time-independent single-particle basis, using the spin-restricted ansatz. Below, we will refer to the basis set $\{|\psi_j\rangle\}$ as the reference basis. The main difference to Hartree-Fock is that M is a parameter of the method, which can be used to control the number of orbitals, and with it the number of configurations and the level of the approximation. M may vary from $\frac{N}{2} = N_\alpha = N_\beta$, which is essentially Hartree-Fock, to N_b, which gives the highest possible number of configurations for a given reference basis and is exact. Before we continue, we would like to note that we cannot simply reuse the matrix elements of the reference basis, but we need to transform the elements in each time step to the time-dependent basis. In almost every situations, this is the most time consuming part of the time propagation, as we need the correct matrix elements to calculate the Hamiltonian (3.14). Due to the higher number of configurations, we are now able to include at least some correlations into our calculations, while we can hopefully use a very small subspace to obtain a good approximation by moving it along with the state vector. This desired behavior is depicted in figure 3.1.

To point out what we have gained with this ansatz, we consider a system with four particles and 50000 reference basis functions—a size that is frequently required to describe processes in atoms. If one calculates the approximated size of one state for CI, one obtains a value in the magnitude of several ten petabyte. For comparison, today's TOP10 supercomputers have a hard drive space [1] in the same

[1] The amount of main memory is no more than in the order of one petabyte.

order of magnitude. That is why we can easily exceed the storage capacity of a state-of-the-art supercomputer by storing only a few states. In comparison, the MCTDHF wavefunction only needs a few hundred megabyte even for larger M. Hence, we can simulated systems which are not even possible with CI with a fraction of the resources. This is especially valid, if we need a large time-independent basis to describe the system, which is almost always the case for atoms.

3.3.2 Equations of motion

After we have described the idea of MCTDHF in the previous section, we will now deduce the equations of motion from the Lagrange formulation of the time-dependent variational principle. This requires a minimization of the action functional

$$S\left[\{C_{\boldsymbol{n}}(t)\},\{\phi_p(t)\}\right] = \int \mathrm{d}t \left\{ \langle\Psi|\,\hat{H} - \mathrm{i}\frac{\partial}{\partial t}\,|\Psi\rangle - \sum_{kl}\mu_{kl}(t)\left(\langle\phi_k|\phi_l\rangle - \delta_{kl}\right)\right\} \tag{3.19}$$

with respect to the variational parameters[2]. The following derivation is mainly inspired by [10]. The Lagrange multipliers are introduced to ensure the orthonormality of the orbitals during the time evolution. The many-particle Hamiltonian $\hat{H}$ used here is essentially the same as the Hamiltonian (3.14). It should be noted, however, that we need to use the matrix elements for the time-dependent basis to account for the additional degrees of freedom.

The minimization of the action function leads to three sets of equations

$$0 = \frac{\delta}{\delta C_{\boldsymbol{m}}} S\left[\{C_{\boldsymbol{n}}(t)\},\{\phi_p(t)\}\right], \tag{3.20}$$

$$0 = \frac{\delta}{\delta\,\langle\phi_p|} S\left[\{C_{\boldsymbol{n}}(t)\},\{\phi_p(t)\}\right] \tag{3.21}$$

and

$$0 = \frac{\delta}{\delta\mu_{ij}} S\left[\{C_{\boldsymbol{n}}(t)\},\{\phi_p(t)\}\right], \tag{3.22}$$

which must be satisfied. Equation (3.22) can be trivially transformed and one gains

$$\langle\phi_i|\phi_j\rangle = \delta_{ij}. \tag{3.23}$$

This is simply the condition for the required orthonormality.

[2] This includes the Lagrange multipliers.

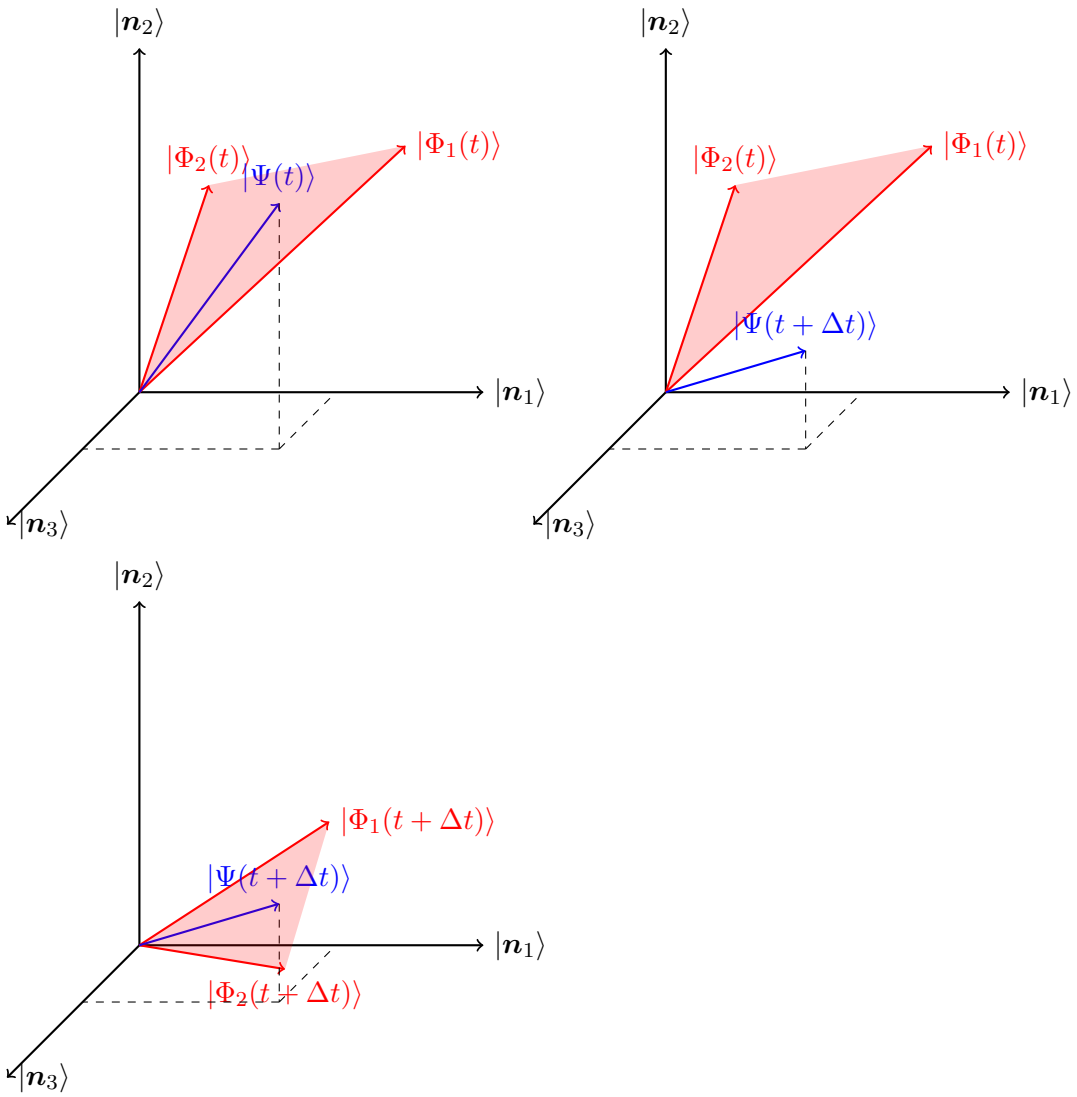

Figure 3.1: Illustration of the time evolution of the exact many-particle state and the MCTDHF subspace. The CI space is spanned by the three configurations $|\boldsymbol{n}_1\rangle$,$|\boldsymbol{n}_2\rangle$ and $|\boldsymbol{n}_3\rangle$, while the initial MCTDHF subspace is spanned by the configurations $|\Phi_1(t)\rangle$ and $|\Phi_2(t)\rangle$. The initial state $|\Psi(t)\rangle$ lies approximately in this subspace. During the time evolution the state leaves the initial subspace, which means it is not well described anymore. To circumvent this, the MCTDHF configurations evolve into new states $|\Phi_1(t+\Delta t)\rangle$ and $|\Phi_2(t+\Delta t)\rangle$ too and span a proper subspace again.

For the derivation of the orbital equations from equation (3.21), we express the expectation value of $\hat{H} - \mathrm{i}\frac{\partial}{\partial t}$ in terms of the density matrices, as per section 2.3.2, and perform the functional derivative. This leads to the set of equations

$$\begin{aligned} 0 = &\left\{ \sum_q D_{pq} \left[\hat{h} - \mathrm{i}\frac{\partial}{\partial t} \right] |\phi_q\rangle + \sum_{qrs} d_{pqrs} \langle \phi_r | \hat{g} | \phi_s \rangle |\phi_q\rangle \right\} \\ &- \sum_q \mu_{pq}(t) |\phi_q\rangle \,. \end{aligned} \tag{3.24}$$

After multiplying equation (3.24) with the projector $|\phi_m\rangle\langle\phi_m|$ and summing over m, we solve for the term which contains the Lagrange multipliers and obtain

$$\begin{aligned} \sum_m \mu_{pm}(t) |\phi_m\rangle = &\sum_m |\phi_m\rangle\langle\phi_m| \\ &\times \left\{ \sum_q D_{pq} \left[\hat{h} - \mathrm{i}\frac{\partial}{\partial t} \right] |\phi_q\rangle + \sum_{qrs} d_{pqrs} \underbrace{\langle \phi_r | \hat{g} | \phi_s \rangle}_{:=\hat{g}_{rs}} |\phi_q\rangle \right\} . \end{aligned} \tag{3.25}$$

Since the left-hand side of equation (3.25) also occurs in equation (3.24), we can insert the former equation into the later, which yields

$$0 = \hat{P} \left\{ \sum_q D_{pq} \left[\hat{h} - \mathrm{i}\frac{\partial}{\partial t} \right] |\phi_q\rangle + \sum_{qrs} d_{pqrs} \hat{g}_{rs} |\phi_q\rangle \right\} . \tag{3.26}$$

$$\hat{P} := \hat{\mathbb{1}} - \sum_{m=1}^{M} |\phi_m\rangle\langle\phi_m| \tag{3.27}$$

is the projector onto the orthogonal complement of the subspace spanned by the orbitals $\{|\phi_m\rangle\}$. Since we would like to solve equation (3.26) for the term involving the time derivative, we need to get rid of the summation over q and the single-particle density matrix elements. We can do this by first multiplying by $\left(\boldsymbol{D}^{-1}\right)_{np}$ and then contracting over the index p. Since this is nothing else than the multiplication of a matrix with its inverse, the density matrix elements and the summation vanishes and we attain

$$\mathrm{i}\hat{P}|\dot{\phi_n}\rangle = \hat{P} \left\{ \hat{h} |\phi_n\rangle + \sum_{pqrs} \left(\boldsymbol{D}^{-1}\right)_{np} d_{pqrs} \hat{g}_{rs} |\phi_q\rangle \right\} \tag{3.28}$$

after solving for the term with the derivative. To eliminate the projector $\hat{P}$ on the left-hand side of equation (3.28), we apply a unitary transformation to the orbitals after which

$$\langle \phi_m | \frac{\partial}{\partial t} |\phi_n\rangle = 0 \tag{3.29}$$

holds. This transformation has two remarkable effects. First, the projector vanishes as anticipated and we reach the orbital equations

$$\mathrm{i}|\dot{\phi_n}\rangle = \hat{P}\left\{\hat{h}\,|\phi_n\rangle + \sum_{pqrs}\left(\boldsymbol{D}^{-1}\right)_{np} d_{pqrs}\hat{g}_{rs}\,|\phi_q\rangle\right\}. \tag{3.30}$$

The second effect is that equation (3.23) is satisfied, if and only if the initial orbitals are orthonormal, since the scalar products of the orbitals are invariants in this case. This can be easily verified by checking

$$\frac{\mathrm{d}}{\mathrm{d}t}\langle\phi_m|\phi_n\rangle = 0. \tag{3.31}$$

Using the product rule one obtains

$$\frac{\mathrm{d}}{\mathrm{d}t}\langle\phi_m|\phi_n\rangle = \frac{\partial}{\partial t}\left(\langle\phi_m|\right)|\phi_n\rangle + \langle\phi_m|\,\frac{\partial}{\partial t}\,|\phi_n\rangle \tag{3.32}$$

and the right-hand side vanishes, because each term is zero due to equation (3.29).

As a last step, we insert expansion (3.18) into equation (3.30) and project the result onto $\langle\psi_k|$ to discretize the equation, after which we arrive at a set equation

$$\mathrm{i}\dot{b}_{nk}(t) = h^{(1)}_{nk}(t) - h^{(3)}_{nk}(t) + \sum_{pqrs}\left(\boldsymbol{D}^{-1}\right)_{np} d_{pqrs}\left(g^{(3)}_{kqrs} - g^{(5)}_{kqrs}\right), \tag{3.33}$$

that determines the time-dependence of the expansion coefficients $b_{nk}(t)$. The quantities

$$h^{(1)}_{nk}(t) = \sum_{j=1}^{N_b} b_{nj}\mathfrak{h}_{jk}(t), \tag{3.34}$$

$$h_{mn}(t) = \sum_{k=1}^{N_b} b^*_{mk}h^{(1)}_{nk}(t), \tag{3.35}$$

$$h^{(3)}_{nk}(t) = \sum_{m=1}^{M} b_{mk}h_{mn}(t) \tag{3.36}$$

and

$$g^{(3)}_{kqrs} = \sum_{j,k,l=1}^{N_b} b_{qj}b^*_{rk}b_{sl}\mathfrak{g}_{ijkl}, \tag{3.37}$$

$$g_{pqrs} = \sum_{i=1}^{N_b} b^*_{pi}g^{(3)}_{iqrs}, \tag{3.38}$$

$$g^{(5)}_{iqrs} = \sum_{p=1}^{M} b_{pi} g_{pqrs} \tag{3.39}$$

in equation (3.30) are variants of the one- and two-particle integrals, which are (partially) transformed to the time-dependent single-particle basis. $\mathfrak{h}_{ij}$ and $\mathfrak{g}_{ijkl}$ denote the elements of the one- and two-particle integrals in the reference basis. As already stated above, we need to use the one- and two-particle integrals in the time-dependent single-particle basis to calculate the many-particle Hamiltonian. These quantities are defined by the equations (3.35) and (3.38).

To obtain the equation for the expansion coefficient in the expansion of the many-particle state (3.17), we calculate the derivative in equation (3.20) and obtain

$$0 = -\mathrm{i}\frac{\partial C_{\boldsymbol{n}}}{\partial t} + \sum_{\boldsymbol{m}} C_{\boldsymbol{m}} \left\langle \boldsymbol{n} \right| \hat{H} - \mathrm{i}\frac{\partial}{\partial t} \left| \boldsymbol{m} \right\rangle . \tag{3.40}$$

The time derivative of the Slater determinants in equation (3.40) vanishes due to condition (3.29), and we finally arrive at the wavefunction equation,

$$\mathrm{i}\frac{\partial}{\partial t}\boldsymbol{C}(t) = \boldsymbol{H}\boldsymbol{C}, \tag{3.41}$$

in vector notation, which takes the same for as the CI equation (3.7). To sum up, we have obtained the wavefunction equation,

$$\mathrm{i}\frac{\partial}{\partial t}\boldsymbol{C}(t) = \boldsymbol{H}\boldsymbol{C}, \tag{3.42}$$

and the orbital equation,

$$\mathrm{i}\dot{b}_{nk}(t) = h^{(1)}_{nk}(t) - h^{(3)}_{nk}(t) + \sum_{pqrs} \left(\boldsymbol{D}^{-1}\right)_{np} d_{pqrs} \left(g^{(3)}_{kqrs} - g^{(5)}_{kqrs} \right), \tag{3.43}$$

as the fully discretized equations of motion for the MCTDHF scheme.

3.3.3 Limiting cases

As already mentioned, the Hartree-Fock method is a special case of the MCTDHF method. We achieve this case, if the number of spin-up particles N_α and the number of particles with spin-down N_β is equal to the number of time-dependent orbitals M, i.e., $N_\alpha = N_\beta = M$. In this case, the expansion (3.17) only consists of a single Slater determinant and the orbital equations transform into the equations of motion for the Hartree-Fock orbitals. The propagation of the wavefunction equation is strictly not necessary, since the only coefficient in the expansion (3.17) assumes the role of a total phase, which does not affect the physical meaning of

the state. A commonly used choice is to the set the coefficient to 1 without loss of generality.

What might be more surprising is the fact that the CI equation is also contained in the MCTDHF equations as a special case. We can understand this, if we chose $M = N_b$ and consider the projector (3.27),

$$\hat{P} := \hat{\mathbb{1}} - \sum_{m=1}^{M} |\phi_m\rangle\langle\phi_m| \,. \tag{3.44}$$

In this case, the basis $\{|\phi_m\rangle\}$ of time-dependent orbitals spans the same Hilbert space as the reference basis $\{|\psi_k\rangle\}$, which especially means that $\sum_{m=1}^{M} |\phi_m\rangle\langle\phi_m|$ is a representation of the identity operator $\hat{\mathbb{1}}$ with regard to this space. As a result, the projector $\hat{P}$ vanishes and therewith the right-hand side of the orbital equation. This means that the orbitals are invariant during the time evolution and we only need to solve the wavefunction equation, which is same as the CI equation.

As a conclusion, MCTDHF handles—at least in theory—the entire range of approximations from the mean-field description of Hartree-Fock to the exact description of CI. The level of approximation can easily be adjusted by varying the number of time-dependent orbitals M.

3.3.4 The FEDVR/spherical harmonic single-particle basis

To be able to perform numerical calculations, we need to choose a suitable single-particle basis. In contrast to the analytic case, where the choice of a basis depends solely on convenience, the proper choice of a basis is an important matter if we truncate the basis expansion, since the structure of the depicted subspace depends on this choice. If the wrong subspace is chosen in this way, the truncation error might be too large to allow physically meaningful simulations. Furthermore, the choice of basis influences the structure of the matrix elements, and thereby the numerical complexity of the algorithms.

To avoid a high numerical complexity, one usually wants to use a preferably small number of basis functions to represent a state. It is therefore a good idea to use basis functions whose structure resembles that of the state. For this reason, one might think that the bound eigenfunctions of the ideal atomic system are a good choice for a basis set. Unfortunately, the answer is not that easy. While the eigenfunctions describe the bound states quite well, we also need a good description of the continuum, since we want to simulate ionization processes. And these states are almost not covered by the bound eigenfunctions. One might argue that one could add the unbound eigenfunctions of the ideal atomic system to the basis to account for the continuum, but this choice would result in a significant numerical complexity.

While we have to discard the idea to use eigenfunction of the ideal atomic system, we can reuse their general structure. Usually one represents the eigenfunctions of an ideal atomic system as a tensor product,

$$|n\rangle \otimes |lm\rangle \,, \tag{3.45}$$

of a radial dimension $|n\rangle$ and an angular dimension $|lm\rangle$. This representation is justified by certain rotational symmetries of the states. As we would not expect that these symmetries are completely vanishing for the interacting atomic system, it would be a good idea to reuse the angular part, while substituting the impeding radial part with something more appropriate for a good representation of the continuum states. The angular states, $|lm\rangle$, are the common eigenstates of the angular momentum operators $\hat{L}^2$ and $\hat{L}_z$, i.e., they satisfy

$$\hat{L}^2 \,|lm\rangle = l(l+1)\,|lm\rangle \tag{3.46}$$

and

$$\hat{L}_z \,|lm\rangle = m\,|lm\rangle \,. \tag{3.47}$$

For the radial dimension, we choose the so called finite element discrete variable representation (FEDVR) basis. As the mathematical definition of the FEDVR basis is rather complex and would go beyond the scope of this work, we will only give a short qualitative description of the functional principle and the advantages of this basis. A detailed discussion can be found in [20].

To construct the FEDVR basis, the spatial extent of the radial dimension is divided into several disjunct elements. In each element several points are chosen to form a grid which can be adapted to a certain application. In our case, we have chosen the so called Gauss-Lobatto grid points. For this grid a set of orthogonal polynomials is calculated in such a way that each grid point corresponds to a sampling point during a Gaussian quadrature [22] with this polynomials. Therefore, the FEDVR scheme acts as a bridge between basis expansions and traditional grid methods. After each of these polynomials are normalized, they are used as a basis within the respective element. To ensure the differentiability of the represented state, the elements are connected by bridge functions. The relation of the grid points and the basis functions is depicted in figure 3.2. The main advantage of the FEDVR basis is that it is spatially localized, which has two major consequences. First, the position operator, and therefore all functions of the position operator, are diagonal, which makes calculations involving these quantities very cheap. For example, the right-hand side of the MCTDHF equations scales linearly with the number of FEDVR basis function N_{rad} due to this fact. The second consequence is that we get a decent representation of the single-particle continuum.

Due to these advantages, the FEDVR/spherical harmonic basis was used during this work in all calculations.

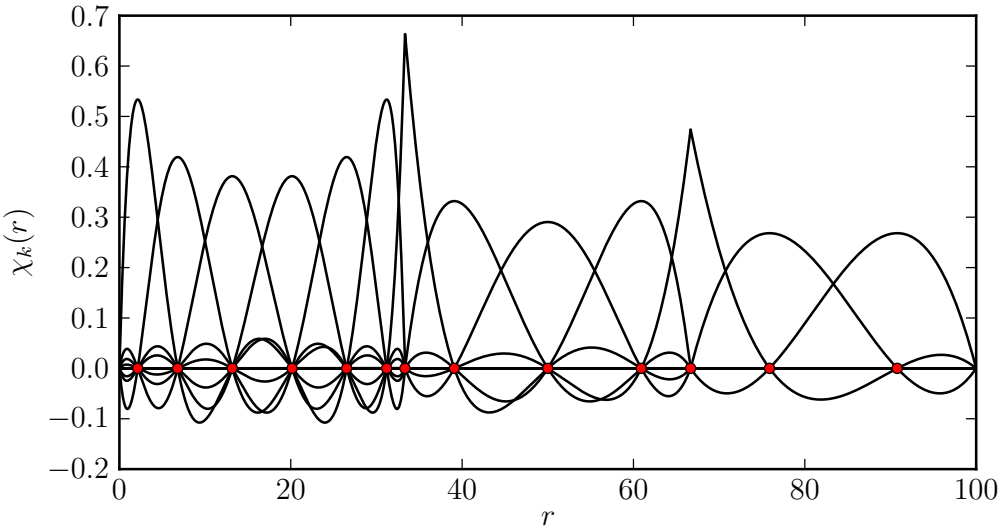

Figure 3.2: Illustration of the FEDVR basis functions for a range of 100 a.u., that is divided into three elements. The elements contain six, four and three basis functions, respectively. The red dots mark the position of the Gauss-Lobatto grid points.

3.3.5 Computational implementation

After we have discussed the theoretical background of the MCTDHF scheme in the previous sections, we will now have a brief insight into the implementation and the improvements, which were made during this work.

The implementation of MCTDHF, which was used throughout this work, is named Kiel MCTDHF, or KMCTDHF for short, and is based on a previous version, developed by Dr. David Hochstuhl. The entire application is written in C++ (according to the C++11 ISO standard). To solve the MCTDHF equation, the application uses an implementation of the DOPR853 integrator, which is based on the implementation in the Numerical recipes [22]. This implementation allows us to use an adaptive step width, based on an error estimation algorithm, and dense output, which can accelerate the propagation and eases the handling, since a suitable step width is automatically chosen. The linear algebra operations, during the calculation of the right-hand side of the MCTDHF equations, are performed with the aid of routines from the linear algebra packages LAPACK, BLAS and Eigen. The current code allows to evolve fermionic systems in time using different basis sets. Before the time propagation is started, the ground state of the system is calculated using the Imaginary Time Propagation (ITP) method. After the

propagation is finished several observables, e.g. momentum, ionization yields and different densities, can be calculated and written to an output file.

A considerable amount of the time during this work was spent on improvements of the application, which were only enabling us to perform many of the calculations, which are discussed in chapter 7. The following is a list of the most important improvements in no particular order:

- A scheme for the prevention of stiffness during the propagation was developed and implemented. This avoidance of stiffness is utterly necessary, since the time propagation would otherwise freeze-up for large basis sets. The application of this scheme gives us usually one or two orders of magnitude of speedup. The scheme is discussed in detail in chapter 4.

- The calculation of the right-hand side of the MCTDHF equations was successfully parallelized, which is discussed in detail in chapter 5. This has allowed us the use the resources of the HLRN to speed up our calculations about another order of magnitude.

- A simple checkpoint system was developed and integrated into the application. The checkpoint system is able to store the current state of the application persistently and to resume the execution from this point on at a later time. This was used during this work to perform calculations, which exceed the 12 hours walltime limit of the HLRN. Unfortunately, the current checkpoint system fails for large basis sets, since two much needs to be stored. This is due to an inherent defect in the structure of the application and should be addressed in future versions.

- The complex arithmetic, which is used throughout the program, was vectorized manually, which gives us a speedup of about 3 on modern processors.

- The hand-crafted binary output format, which was previously a persistent source of difficulty, was substituted with a more stable one, which is based on the established HDF5 format [23]. In addition, this results in an easier and more versatile access to the stored data, and allows to access the data through other languages, most notably Python.

- A proper build system, based on CMake, was created, which allows us to build the application on different computers without the need to manually reconfigure everything. Most notably, this allows us finally to properly build the application on the HLRN.

- The instable time propagation module was rewritten from scratch. This issue was also blocking the integration of the checkpoint system.

- The dependency on the GNU Scientific Library was eliminated[3]. This was done preemptively to avoid future problems, since the library does not seem to be maintained anymore.
- A new user interface was introduced, which gives a much more fine-grained access to several quantities.

In addition, many minor fixes and improvements were applied to the program during this work. Together, all performance improvements produce a significant speedup within the range 30 to 10000 and enable the subsequent complex simulations in the first place.

While the application has been greatly improved during this work, there is much to do for future versions. For example, the algorithms are not optimized for modern processors and the execution of the algorithms is stalled due to heavy access of the slow main memory. An optimization of the memory access pattern would allow for another speedup of an order of magnitude. Another idea would be to use accelerators, like CUDA-enabled GPUs, to speed up the execution.

[3]Thanks to the help of David Hochstuhl.

4 Stiffness reduction

In this chapter, we will devote ourself to the issue of stiffness which prevents to apply the MCTDHF equations to complex systems. In the first part of the chapter, we will discuss the root cause of the problem and then present several methods which are commonly applied to this problem. In the second part, we will propose a domain-specific solution for this problem and outline a possible implementation.

4.1 Introduction

During the course of this work, we observed that the step size, which was used for the numerical integration of the MCTDHF equations, decreases, if we increase the size of the used basis set. This phenomena is pictured in figure 4.1 for atomic helium. Due to its simplicity, we will use helium as the test case throughout this chapter, using the FEDVR/spherical harmonic basis for the numerical description. The radial basis extends over a range of 100 a.u. divided into 25 finite elements. The magnetic quantum number m is 0 for all basis functions throughout this chapter. The entire system is always propagated over a time range of 150 a.u. without any excitations. Since we did not change the physical system, this cannot be a property of the solution and must be a result of the numerical description. Such behavior, where the step size is determined by other factors rather than the solution, are commonly known as stiffness [22] in computational science. To illustrate the origin of the stiffness, we consider the time-dependent Schrödinger equation

$$\mathrm{i}\frac{\partial}{\partial t}\left|\Psi(t)\right\rangle = \hat{H}\left|\Psi(t)\right\rangle \tag{4.1}$$

with a time-independent Hamiltonian $\hat{H}$. As commonly known, the solution of (4.1) can always be written as an expansion

$$\left|\Psi(t)\right\rangle = \sum_k c_k e^{\frac{\mathrm{i}}{\hbar}E_k t}\left|E_k\right\rangle \tag{4.2}$$

of the state $|\Psi(t)\rangle$ into energy eigenstates $|E_k\rangle$ with some initial expansion coefficients c_k. In numerical calculations, all eigenstates are always at least weakly occupied due to rounding errors, hence all eigenstates contribute to the solution. Despite the low occupancy of eigenstates with large energy eigenvalues in physical

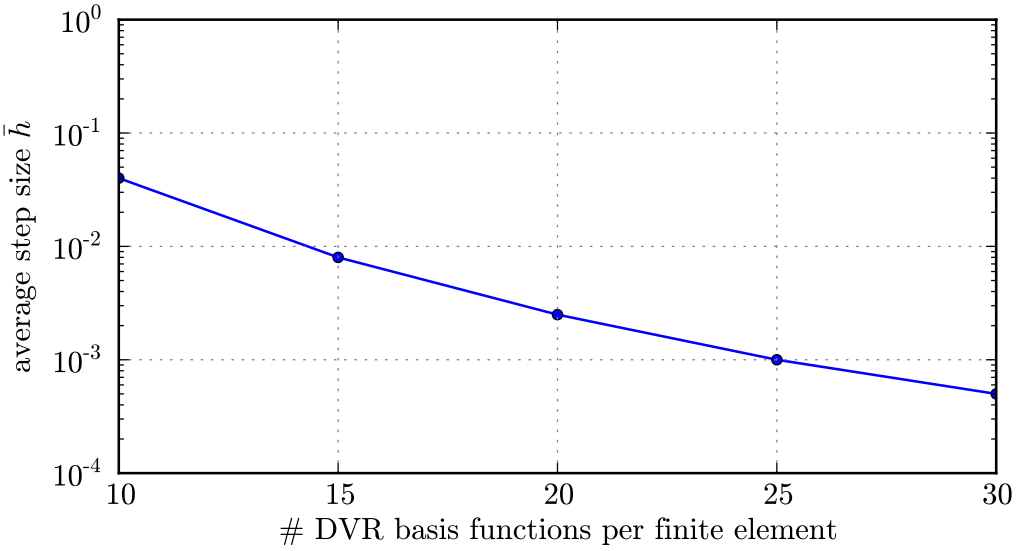

Figure 4.1: Dependency of the step size on the number of DVR basis function per finite element without stiffness reduction. The angular basis contains spherical harmonics with azimuthal quantum numbers l up to 2.

systems due to the lack of strong enough excitations, the used integration algorithm tries to resolve the highly-oscillating terms, which correspond to these eigenstates, in the expansion (4.2). According to the Nyquist–Shannon sampling theorem the maximal step size which can be used to resolve the oscillations is $h_{\max} \propto \frac{1}{E_{\max}}$, where $E_{\max}$ is the largest absolute value of any of the E_k. If this condition is not satisfied, an explicit integration scheme would become numerical unstable. The used integrator with adaptive step size, adjusts the step size accordingly to prevent this instability. In the case that we increase the size of the basis set and keep all physical parameters of the system constant, $E_{\max}$ starts to rise and the step size has to be consequently decreased, resulting in the observed effect. In the following we will examine several possible methods to prevent the effect of the stiffness.

4.2 Prior art

The natural approach to counter the numerical instability of explicit integrators is the application of stable algorithms. Some implicit integration schemes, such as implicit Runge-Kutta methods or BDF-integrators, are know to exhibit this property by damping the occurring errors, instead of accumulating them [22]. The common downside of these methods compared to explicit methods is that one

needs to solve a system of equations in every integration step, which in the worst case might be non-linear. In either case, commonly used implementations need to calculate the Jacobian matrix

$$J := \left(\frac{\partial f_i(x_1, \ldots, x_n)}{\partial x_j} \right) \tag{4.3}$$

of the system function f repeatedly during the integration process. For the MCTDHF method, we expect that the evaluation of the Jacobian would the most time consuming part of an implicit integration scheme. Therefore, we will focus on the problem of its evaluation in the following.

One way to evaluate a Jacobian is the analytical calculation of the involved derivatives and the subsequent implementation of the analytical expressions as a part of the algorithm. While this method provides the exact Jacobian—up to rounding errors during the evaluation—, it is also error-prone for complex systems due to human involvement in the evaluation process. Even if the Jacobian is implemented correctly during the first implementation, each subsequent change to the system function needs to be carefully adapted and replicated in the Jacobian, off-loading continuous, non-trivial maintenance burden onto the developer. Even during the first implementation, the additional workload can be significant for complex system functions, since in most cases the Jacobian is—implementation-wise—at least as complex as the system function itself, which would at the minimum double the effort. The textbook method to circumvent these problems is the use of finite differences [22, 24], which approximate the derivatives numerically. Since the evaluation of the finite differences requires the repeated evaluation of the system function for different arguments only, most of the already available implementation can be reused, making the implementation sufficiently cheap. On the other hand, finite differences suffer from some well-known numerical problems [24], precisely truncation errors and subtractive cancellation, which might introduce a hardly controllable error source into the algorithm. In addition highly accurate approximations often require the application of higher-order finite differences, for which the system function needs to be evaluated more often, raising the amount of needed computational resources. A scheme, which is frequently used to calculate the Jacobian, while evading the aforementioned problems, is the automatic differentiation [25,26], which combines the good numerical properties and cheap evaluation of the analytical differentiation with the possibility to automatize most of the implementation process. The downside of this method is that most automatic differentiation software requires the annotation of the source code of the system function or some other changes in the program. While the effort is much smaller than the time spent during the implementation of the analytic approach, this should be considered, if one chooses a method.

Even if we are able to theoretically calculate the Jacobian, we would need to

populate all of its elements, scaling with the square of the number of variables. For our purposes the number of elements is $M \cdot N_b$, which ranges from a few variables to several hundred thousands in typical simulations. The calculation of each element would require to evaluate the system function at least once. Under the consideration that the system function is by far the most expensive part of an MCTHDF calculation, the runtime of the program would be greatly increased by the application of an implicit method for more complicated systems. The increased runtime usually limits the number of variables to the region of a few hundred to a few thousand, depending on which integrator is applied. Since this restricts the entire algorithm to simple systems, while greatly increasing the time spent on the implementation, we consider this approach impractical for our purposes.

4.3 Energy subspace projection method

In this section, we will propose the Energy subspace projection (ESP) method as a means to solve the stiffness issue at its root. The application of a domain-specific scheme allows a much handier approach than more generic methods.

4.3.1 Introduction

To avoid the aforementioned problems of the generic methods described in the previous section, we propose a domain-specific solution, the energy subspace projection (ESP) method[1], as a possible solution. The major advantage of such an approach over a fully generic method is that one can tailor the scheme to the specific structure of this domain, which often makes the solution more suitable. As already shown in section 4.1, the root cause of the stiffness are the high energy eigenvalues in the Hamiltonian. Since the corresponding expansion coefficients are—due to their non-physical origin—small in the majority of cases, it is a valid approximation to truncate the expansion (4.2) by discarding these coefficients. This directly eliminates the highly-oscillating terms in Eq. (4.2). From a linear algebra perspective, truncation is a projection onto the subspace spanned by the energy eigenvectors with desired eigenvalues, hence the name of the method. To our best knowledge, this is the first time that such a method was applied to a quantum mechanical problem.

As a simplification, we will first develop the method by applying our idea to the time-dependent Schrödinger equation

$$\mathrm{i}\frac{\partial}{\partial t}\boldsymbol{c} = \boldsymbol{H}\boldsymbol{c}, \tag{4.4}$$

[1] This method was developed in collaboration with Dr. David Hochstuhl.

which was discretized using an arbitrary basis of size N_b, before we try to incorporate the scheme into the much more complex MCTDHF algorithm.

To proceed, we need to identify the spurious eigenvalues and their associated coefficients. In the general case this would require a quite sophisticated scheme, since one has to consider the occupation of the eigenstates, as we only can discard the lowly occupied states safely. Since in practice all energy levels above a certain threshold are lowly occupied, we decided to rely on the user to pick a suitable energy threshold E_{cutoff}, hence known as cutoff energy, using his knowledge of the physical system. While this method might ignore some of the spurious eigenvalues, the implementation is greatly simplified by this choice and performs quite well for all practical purposes. In what follows, it is assumed that the energy eigenvalues are sorted in increasing order. In practice this is not an issue, since almost all linear algebra tools already calculate the eigenvalues in this order. Due to the order the cutoff energy directly corresponds to an index N_c for which the property

$$i \in [0, N_c] \iff E_i < E_{\text{cutoff}} \tag{4.5}$$

holds. It should be noted that we ignore the problem of negative eigenvalues with a large absolute value at this point, as we will see in section 4.3.3 that this case is difficult to handle and has barely any practical relevance. Using this cutoff index N_c, one can now define the truncation matrix $\tilde{\boldsymbol{L}}$, which reads

$$\tilde{\boldsymbol{L}} := \begin{pmatrix} \mathbb{1}_{N_c \times N_c} & 0 \\ 0 & 0 \end{pmatrix} \tag{4.6}$$

in block matrix representation. If applied to the coefficient vector $\tilde{\boldsymbol{c}}$, the truncation matrix precisely sets the spurious coefficients to zero, while preserving the desired coefficients. Since the expression $\mathbb{1} - \tilde{\boldsymbol{L}}$ will be used frequently below, it is convenient to define it as the remainder matrix

$$\tilde{\boldsymbol{R}} := \mathbb{1} - \tilde{\boldsymbol{L}}. \tag{4.7}$$

Since we apply these matrices to quantities which are represented in our arbitrarily chosen basis, we need to transform them back from the basis of energy eigenfunctions into the chosen basis via their corresponding basis transformation $\boldsymbol{V}$, which leads to the expressions

$$\boldsymbol{L} := \boldsymbol{V}^\dagger \tilde{\boldsymbol{L}} \boldsymbol{V} \tag{4.8}$$

and

$$\boldsymbol{R} := \boldsymbol{V}^\dagger \tilde{\boldsymbol{R}} \boldsymbol{V}. \tag{4.9}$$

Using the identity

$$\mathbb{1} = \boldsymbol{L} + \boldsymbol{R} \tag{4.10}$$

the right-hand side of equation (4.4) can be rewritten as

$$\boldsymbol{H}\left(\boldsymbol{L}+\boldsymbol{R}\right)\boldsymbol{c}=\boldsymbol{H}\boldsymbol{L}\boldsymbol{c}+\boldsymbol{\rho}(\boldsymbol{c}) \tag{4.11}$$

with a remainder term

$$\boldsymbol{\rho}(\boldsymbol{c})=\boldsymbol{H}\boldsymbol{R}\boldsymbol{c}. \tag{4.12}$$

If we discard the remainder term in equation (4.11), we have already achieved our goal to eliminate the spurious eigenvalues. The success of our approach can easily be verified on the helium test system, as shown in the figures 4.2 and 4.3. As we see, the average step size remains constant, even if we increase the size of the basis set. The effect on the runtime is depicted in figures 4.4 and 4.5, which show that we gain a significant speedup of over an order of magnitude for large basis sets due to the reduced stiffness of the system. Figure 4.6 illustrates that the average step size is actually proportional to the inverse maximal energy—which should be roughly the cutoff energy—as already mentioned in section 4.1. The plateau for small energies exists due to other effects like the real variation of the solution which demands a certain step size. This value will be even larger if we increase the size of the basis set further to treat more complex systems than helium. The implementation of the algorithm which we used to produce this results is described in section 4.3.3.

4.3.2 Error analysis

Since the ESP scheme is an approximate procedure, it is important that we have an understanding of the circumstances under which we can apply this scheme without compromising the accuracy of our calculations. The only additional error source in the ESP method is the truncation, which is described by the remainder term (4.12). Using any vector norm $\|.\|$ and a corresponding compatible matrix norm, we can deduce the following estimate for the truncation error,

$$\begin{aligned}\epsilon(\boldsymbol{c}) &= \|\boldsymbol{\rho}(\boldsymbol{c})\| \\ &= \|\boldsymbol{H}\boldsymbol{R}\boldsymbol{c}\| \\ &\leq \|\boldsymbol{H}\|\|\boldsymbol{R}\boldsymbol{c}\| \\ &= \|\boldsymbol{H}\|\|\boldsymbol{V}^{\dagger}\tilde{\boldsymbol{R}}\boldsymbol{V}\boldsymbol{c}\| \\ &= \|\boldsymbol{H}\|\|\tilde{\boldsymbol{R}}\tilde{\boldsymbol{c}}\|,\end{aligned} \tag{4.13}$$

from the remainder term. The expression $\|\tilde{\boldsymbol{R}}\tilde{\boldsymbol{c}}\|$ exposes that the error is solely determined by the eliminated expansion coefficients. Therefore, the approximation remains valid as long as all truncated eigenstates are only lowly occupied, as we have already expected.

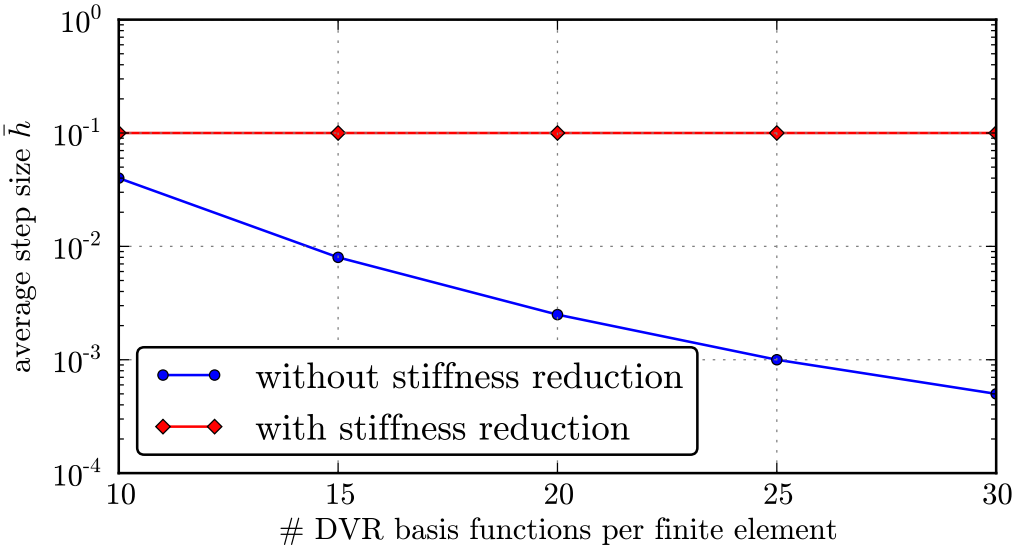

Figure 4.2: Dependency of the step size on the number of DVR basis functions per finite element with and without stiffness reduction. The angular basis contains spherical harmonics with azimuthal quantum numbers l up to 2.

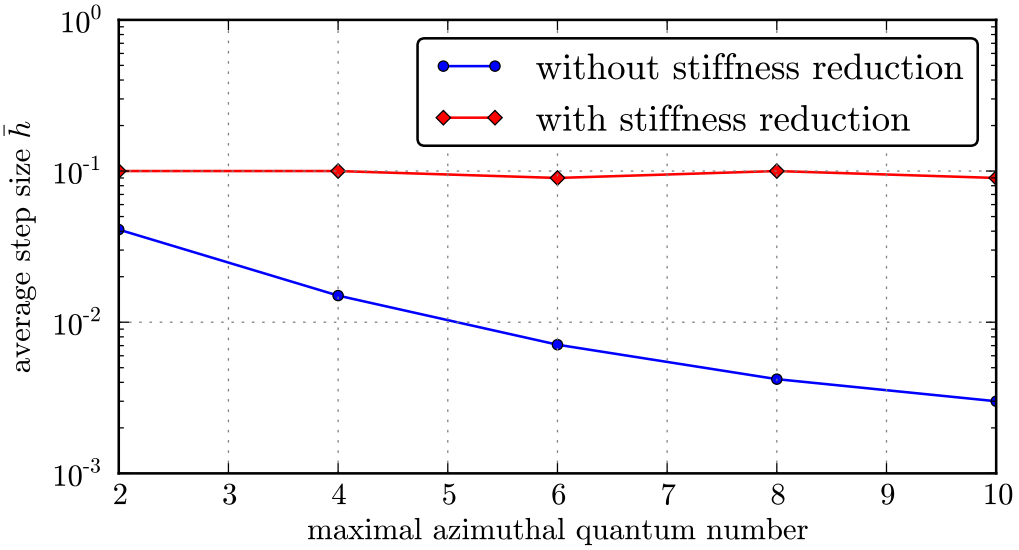

Figure 4.3: Dependency of the step size on the maximal azimuthal quantum number $l_{\max}$ with and without stiffness reduction. Each finite element contains 10 DVR basis functions.

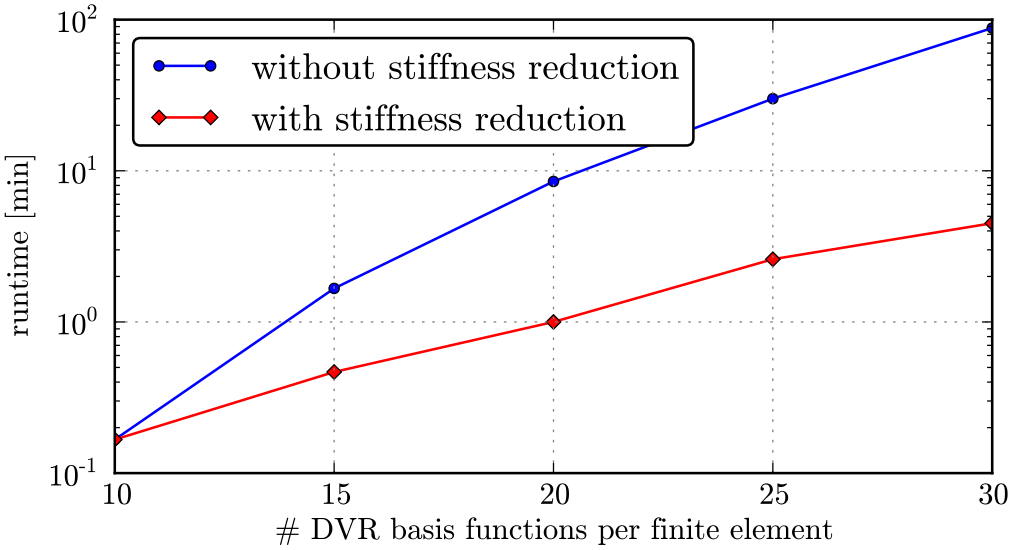

Figure 4.4: Dependency of the runtime on the number of DVR basis functions per finite element with and without stiffness reduction. The angular basis contains spherical harmonics with azimuthal quantum numbers l up to 2.

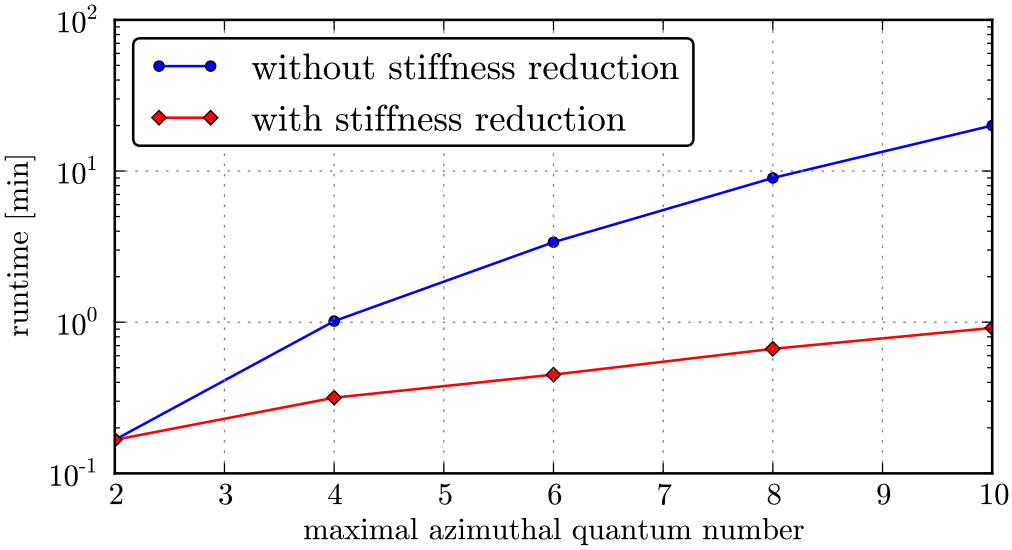

Figure 4.5: Dependency of the runtime on the maximal azimuthal quantum number $l_{\max}$ with and without stiffness reduction. Each finite element contains 10 DVR basis functions.

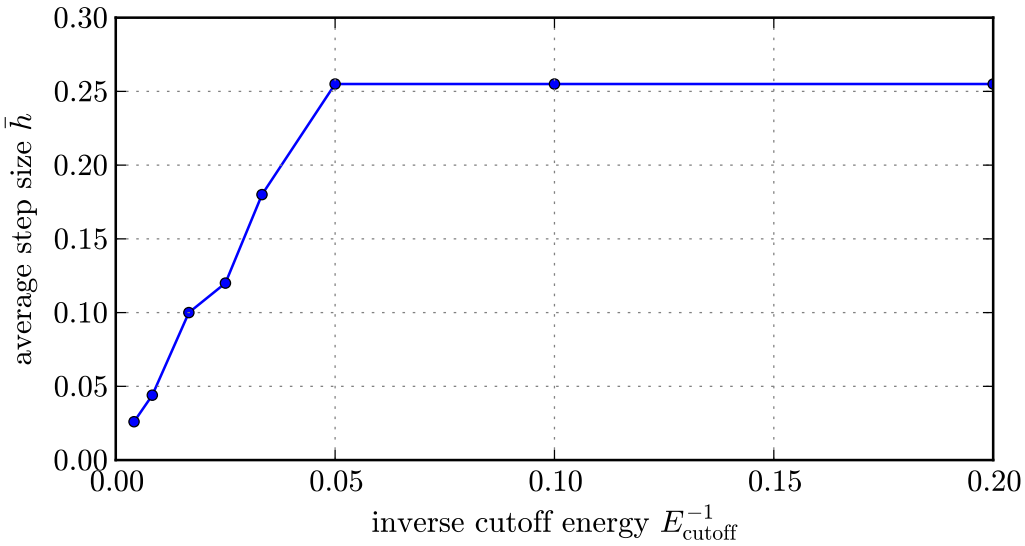

Figure 4.6: Dependency of the step size on the inverse cutoff energy. The angular basis contains spherical harmonics with azimuthal quantum numbers l up to 4.

Error estimators like (4.13) are good to get an intuition for the error source and are often necessary to develop more sophisticated schemes. Though, it is often not viable to use them as a method to obtain the error in practice, since in most cases not all quantities are known or are at least not feasible to calculate. Therefore, it is necessary to perform empirical tests to explore the real error properties. We have performed these tests for the helium test system using different metrics for the induced error. The first metric used is the difference between the ground state energy for some value of E_{cutoff} and the ground state energy in the exact limit $E_{\text{cutoff}} \to \infty$. The dependency of this metric on the cutoff energy is shown in figure 4.7. We can see that the error remains small until the cutoff energy reaches the energy 40 a.u., which roughly corresponds to the point after which higher occupied energy eigenstates are purged. After this point, the error starts to rise rapidly as we purge more and more occupied energy eigenstates. Since the maximal eigenvalue of the Hamiltonian is usually significantly larger than 40 a.u., it is evident that we can considerably reduce the stiffness without having to trade off accuracy for performance. The L_2 error

$$\| \, |\psi_{E_{\text{cutoff}}}\rangle - |\psi_{\infty}\rangle \, \|_2 \tag{4.14}$$

of the state at the end of the propagation, which we use as a second error metric, shows a quite similar behavior, as we can deduce from figure 4.8. Another feature

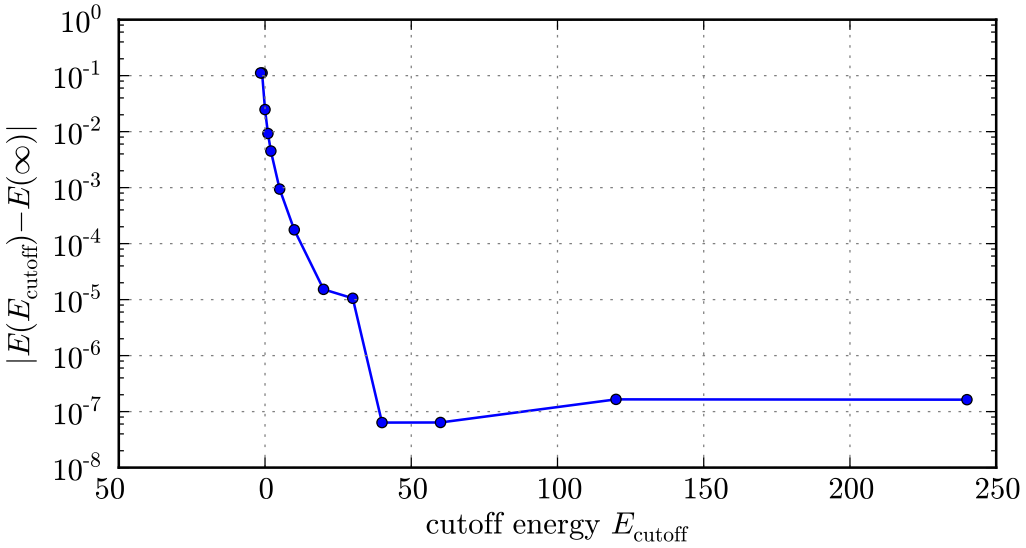

Figure 4.7: Error in the ground state energy in dependency of the cutoff energy E_{cutoff}. Each finite element contains 15 DVR basis functions. The angular basis is constructed from spherical harmonics with azimuthal quantum numbers l up to 4.

shown in figure 4.8 is the comparison of the total error compared to the pure error in the phase. It is evident that the error in the normalization can be neglected in comparison to the error in the phase. The phase error was calculated by explicitly normalizing the densities before the L_2 error is calculated. While it is true that we can ignore the normalization error in most cases, it should be noted that this might not be true, if the propagation time is very long, since the normalization decreases during every time step due to the truncation. In these cases, one should account for the error by either explicitly normalizing the state or by taking into account the error during the calculation of all observables.

4.3.3 Implementation

In this section, we will cover the more technical aspects of the ESP method, and its application to the MCTDHF equations. While we will restrict the discussion to the MCTDHF equations, some aspects of the implementation might be valuable even for more general cases. Since the stiffness—at least in the MCTDHF scheme—results from large eigenvalues in the single-particle Hamiltonian, we need to apply the ESP scheme to the orbital equation. Although this equation does not exactly have the form of (4.1), it is similar enough for a successful application. From a

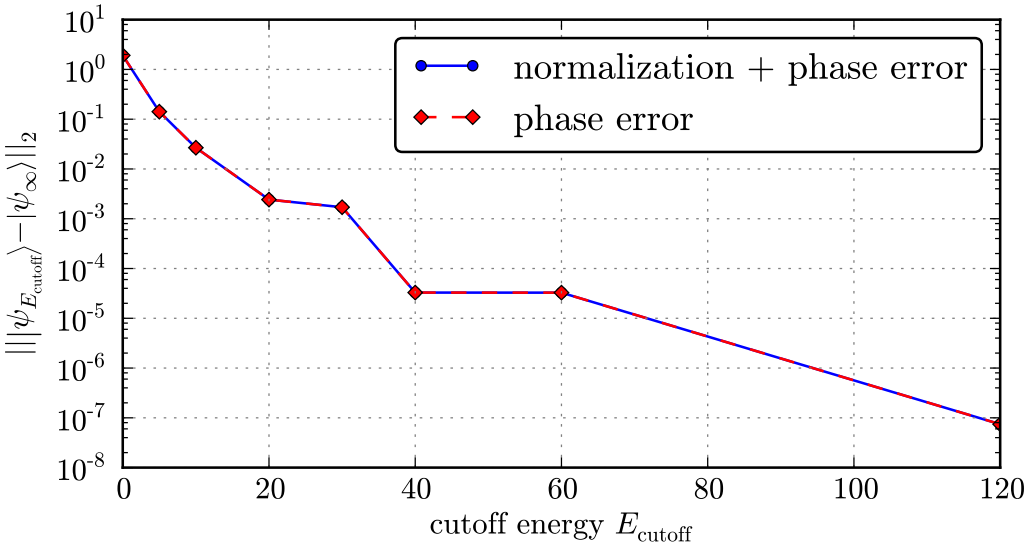

Figure 4.8: L_2 error of state at the end of the propagation with respect to the cutoff energy E_{cutoff}. Each finite element contains 15 DVR basis functions. The angular basis constructed from spherical harmonics with azimuthal quantum numbers l up to 4.

practical point of view, it is convenient to apply the truncation matrix $\boldsymbol{L}$ either to the Hamiltonian or to the orbital expansion coefficients. Since this would simply result in a new Hamiltonian or new expansion coefficients, we can reuse the existing code for the calculation of the right-hand side of the MCTDHF equations in this case. We chose to apply the truncation matrix to the expansion coefficients for two reasons. First, the Hamiltonian is time-dependent in many common cases of use of the MCTDHF scheme. Therefore, we would need to reapply the truncation matrix to the Hamiltonian in every time step, which encloses at least the costly evaluation of one matrix-matrix product. Hence, we only recommend this approach if the Hamiltonian is time-independent and we can reuse the evaluated product. The second reason is the fact that the orbital equation does also contain other terms apart from the one-particle contributions [20]. If we would apply the truncation matrix solely to the single-particle Hamiltonian, we would introduce an inconsistent approximation to the equation. In theory, one could apply the scheme to all operators within the orbital equation consistently, but this is much more demanding than the application to the expansion coefficients, since we would need to evaluate complex tensor contractions. On the other hand, the application of the truncation matrix on the expansion coefficients only involves a cheap matrix-vector product and the approximation is consistently included in

every term automatically. Let $\boldsymbol{b}_j$ be the expansion coefficient vector of the j-th orbital, then the new coefficients read

$$\boldsymbol{b}'_j = \boldsymbol{L}\boldsymbol{b}_j. \tag{4.15}$$

To speedup the computation of (4.15), we can exploit the structure of the truncation matrix $\boldsymbol{L}$. If we only discard a few eigenvalues, the truncation matrix in the energy representation (4.6) has merely a few non-zero entries. After inserting the definition (4.8) of $\boldsymbol{L}$ into equation (4.15), which results in the expression

$$\boldsymbol{b}'_j = \boldsymbol{V}^\dagger \tilde{\boldsymbol{L}} \boldsymbol{V} \boldsymbol{b}_j, \tag{4.16}$$

we can insert another $\tilde{\boldsymbol{L}}$, obtaining

$$\boldsymbol{b}'_j = \boldsymbol{V}^\dagger \tilde{\boldsymbol{L}} \tilde{\boldsymbol{L}} \boldsymbol{V} \boldsymbol{b}_j. \tag{4.17}$$

This is possible, because

$$\tilde{\boldsymbol{L}}^2 = \tilde{\boldsymbol{L}} \tag{4.18}$$

holds for the truncation matrix $\tilde{L}$. Applying the truncation matrix on one transformation matrix each, we can rewrite (4.17) as

$$\boldsymbol{b}'_j = \left(\boldsymbol{V'}^\dagger \left(\boldsymbol{V'} \boldsymbol{b}_j \right) \right) \tag{4.19}$$

with

$$\boldsymbol{V'} = \tilde{\boldsymbol{L}} \boldsymbol{V}. \tag{4.20}$$

$\boldsymbol{V'}$ is an $N_c \times N_b$ matrix effectively, since most of the elements of $\boldsymbol{V}$ are set to zero by $\tilde{\boldsymbol{L}}$. If we apply this matrix to the coefficient vector according to the associativity implied by (4.19) we can reduce the computational cost from N_b^2 to $2N_cN_b$.

In the case of only a few discarded eigenvalues, we can apply a similar scheme by substituting $\boldsymbol{L}$ using

$$\boldsymbol{L} = \mathbb{1} - \boldsymbol{R} \tag{4.21}$$

and subsequently applying the same decomposition to $\boldsymbol{R}$. This leads to the equation

$$\boldsymbol{b}'_j = \left(\mathbb{1} - \boldsymbol{V''}^\dagger \boldsymbol{V''} \right) \boldsymbol{b}_j = \boldsymbol{b}_j - \left(\boldsymbol{V''}^\dagger \left(\boldsymbol{V''} \boldsymbol{b}_j \right) \right) \tag{4.22}$$

with

$$\boldsymbol{V''} = \tilde{\boldsymbol{R}} \boldsymbol{V}, \tag{4.23}$$

which can be easily evaluated in a similar manner.

As already mentioned above, the handling of negative energies with large absolute values was discarded to simplify the implementation, since such values never

occurred during this work. The explanation for this phenomena is that the ground state energy of the single-particle Hamiltonian provides—by definition—a lower bound for all energy eigenvalues. A fast estimation for atomic systems shows that the ground state energy lies within the energy range specified by typical cutoff energies E_{cutoff} except for heavier atoms and ions. Using the absolute value of the ground state energy of a hydrogen-like system

$$|E_0| = \frac{Z^2}{2} \tag{4.24}$$

one arrives at the condition

$$|E_0| = \frac{Z^2}{2} \leq E_{\text{cutoff}} \tag{4.25}$$

for allowed atomic numbers Z. The maximal value of Z, which satisfies (4.25) is

$$Z_{\max} = \lfloor \sqrt{2E_{\text{cutoff}}} \rfloor. \tag{4.26}$$

During most of this work a cutoff $E_{\text{cutoff}} = 60 \approx 1640$ eV was chosen, which corresponds to a maximal atomic number $Z_{\max} = 10$. Since such large systems are out of the scope of this work, we ignore this problem for now. Another point which should be considered is that the negative energy levels are highly occupied, if one starts from the ground state. Therefore, the ESP scheme—at least in its current form—would not be applicable in this common case anyway.

4.4 Summary and extensions

In the preceding sections, we were able to pinpoint the origin of the stiffness and developed a scheme, which is able to eliminate the stiffness, while avoiding the high costs of implicit integration methods. In addition, we were able to show that the truncation error introduced by this scheme can be neglected for most practical purposes if the threshold for the truncation is chosen accordingly. To conclude this chapter, we give some possible extensions, which might enhance the scope or increase the practicality of the method in different situations:

- While we decided to use a quite simple scheme to select the eliminated eigenvalues, one could imagine more sophisticated methods. For example, one could use the error estimator, which was presented in 4.3.2, to incrementally purge energy eigenfunctions, from the lowest occupied to the highest occupied, as long as a user-specified error bound is undershot. This would allow the application of the method to systems with strongly changing occupations over a large region of energies or systems where the spurious eigenvalues are positioned between desired ones.

- Another improvement would be the restriction of the projector to a specific subspace. This can be important for large Hilbert spaces, if the spurious eigenvalues are only originating from a very small subspace. Therefore, it would be a waste of computational resource, to apply the scheme to the entire Hilbert space. A classic example is the description of atomic systems with localized basis sets, where the basis function lie very dense in the small core region. On the other hand, the basis functions in the larger outer part of the space lie relatively sparse and do not contribute to the stiffness, while spanning the largest part of the Hilbert space. An experimental implementation of this feature shows very promising results for such systems.

5 Parallelization

In this chapter, we will outline a possible parallelization scheme for the MCTDHF equations and introduce the necessary tools to explore its characteristics. In the last part of this chapter, we will perform such a survey and will discuss the consequences.

5.1 Motivation

While the ESP method described in chapter 4 tries to accelerate the MCTDHF scheme by improving the algorithm, a much more direct approach to accelerate the application would be the use of more computational resources in the form of parallelization. Due to the fact that virtually every modern computer has several processing units, parallelization is getting more and more important—even outside of the traditional high-performance computing (HPC) field—, since a serial program would waste valuable resources. As most cluster computers are distributed-memory systems—including our main cluster, the HLRN—we will focus on this kind of parallelization. While we can only give a short introduction into the field of parallelization due to spatial and temporal constrains, we deem the results too important to be ignored.

5.2 The algorithm

During this work, we have implemented a parallelization scheme[1] for distributed-memory clusters using the well-known Message Passing Interface (MPI). The basic idea of the scheme is the parallel calculation of all two-particle quantities during a time step. This is possible since all two-particle are 4-tensors of the form A_{pqrs} and computations regarding different values of the multi-index (rs) are completely independent of each other. Hence, we can trivially distribute the work over all processes, by splitting the computation of all tensors over the multi-index (rs). The only common dependency of all computations is the current state, which can be easily distributed to all processes at the beginning of a time step. To perform the computations, the set of processes is divided into a master process which controls the execution of all code and several worker processes which only perform parallel

[1] This scheme was developed in collaboration with Dr. David Hochstuhl.

computations. During the execution of a parallelized region of code, the master node behaves in the same way as a worker node. The application of this scheme leads to the following steps, which are performed during each time step:

1. Broadcast the current state from the master process to all worker processes.
2. Calculate all single-particle quantities within the master process.
3. Transform the electron integrals partially within every process in parallel.
4. Calculate the two-particle contributions of the orbital and wavefunction equation partially within every process in parallel.
5. Reduce all partially calculated two-particle contributions within the master process. This yields the full two-particle contributions.
6. Combine the one-particle and two-particle contributions.

After the last step, the MCTDHF equations are integrated within the master process and the algorithm starts again at the first step.

5.3 Performance metrics

Since we cannot observe the behavior of a parallelized application in real time, we need metrics which allow us to perform a post-mortem analysis of the algorithm. In the following sections, we will present some metrics, which are commonly applied during the empirical analysis of parallel algorithms. An ubiquitous quantity in these calculations is the speedup

$$S(n,p) := \frac{T(n,p)}{T(n,1)}, \tag{5.1}$$

which is defined as the ratio of the runtime $T(n,p)$ of the algorithm for a given problem size n on p processors and the runtime $T(n,1)$ of the algorithm for the same size on one processor.

5.3.1 Strong scaling and Amdahl's law

One of the first proposed use cases for parallel algorithms was the reduction of the runtime, which was needed to solve a given problem by applying more computational resources. The property of an algorithm which is coupled with this use case is the so called strong scaling behavior. Strong scaling behavior is defined as the behavior of $S(n,p)$ regarding p for $n = \text{const}$. That a good strong scaling

behavior is not a goal which can be easily achieved gets evident if one examines Amdahl's law [27]

$$S(n,p) \leq \frac{1}{f(n) + \frac{1-f(n)}{p}}, \tag{5.2}$$

a model for the strong scaling behavior of parallel algorithms proposed by Amdahl in 1967. Here $f(n)$ denotes the inherently serial fraction of the sequential program. For a large number of processors—which is the interesting use case for parallel algorithms— the right-hand side of equation (5.2) behaves almost like $\frac{1}{f}$ as a function of the serial fraction. Due to the sharp slope of $\frac{1}{f}$ around $f = 0$, even a slight increase in the serial fraction will restrict the speedup to a very small value. Hence it is a very demanding task to apply this approach to most problems, except for the most simple ones.

5.3.2 Weak scaling and Gustafson's law

To counter the problems, which are implied by Amdahl's law, Gustafson proposed a different point of view on parallel algorithms in 1988 [28]. His argument is that in most use cases the problem size is not restricted by external means, therefore we could increase the problem size, while we apply more resources to keep the time, which is needed to solve the problem, constant. This leads to the notion of the weak scaling behavior which is defined as the behavior of $S(n,p)$ regarding p for some problem size $n(p)$ satisfying $\frac{n(p)}{p} = \text{const}$. The weak scaling behavior of a parallel algorithm can be modeled by Gustafson's law,

$$S(n,p) \leq p + s(n,p)(1-p), \tag{5.3}$$

where $s(n,p)$ denotes the serial fraction of the parallel algorithm. Due to the linear slope of the right-hand side of equation (5.3), Gustafson's law is much more forgiving in comparison to Amdahl's law if we introduce serial parts into a parallel algorithm. Due to this fact, this approach to parallelism seems very promising to us. Since we can always increase the size of our basis sets to get a more accurate description or to simulate more complex system we should always be able to use this approach.

5.3.3 Karp-Flatt metric

Since both Amdahl's law and Gustafson's law do not include effects due to parallel overhead, Karp and Flatt proposed the Karp-Flatt metric [29]

$$e(n,p) = \frac{\frac{1}{S(n,p)} - \frac{1}{p}}{1 - \frac{1}{p}} \tag{5.4}$$

an empirical metric for the serial fraction which can be used to expose such effects.

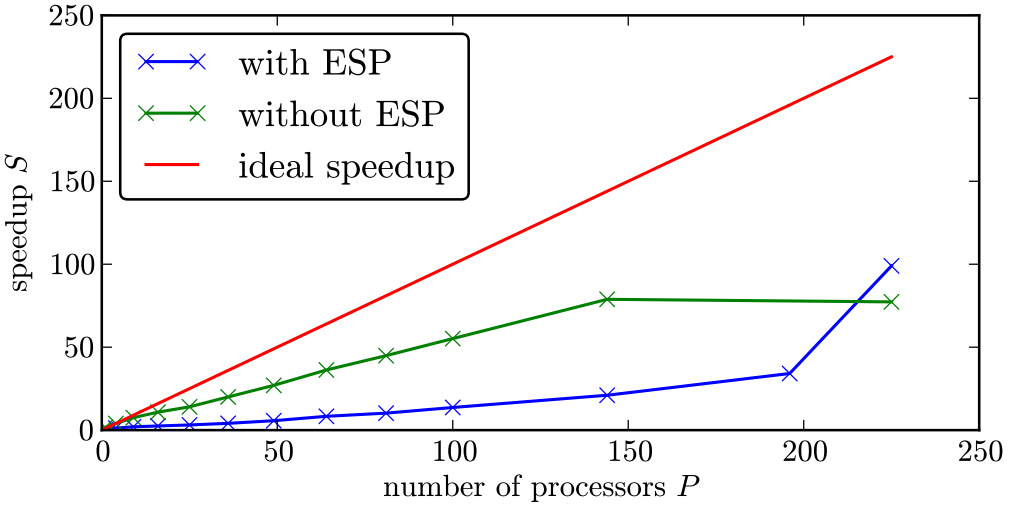

Figure 5.1: Comparison of the speedups for the test system with the ideal speedup with and without the application of the ESP scheme. The algorithm was executed in a weak scaling fashion.

5.4 Performance measurements

To test the behavior of our implementation on a real system, we used atomic helium as a test system. The ground state was propagated over 100 a.u. without any excitation. The FEDVR/spherical harmonics basis was used for the numerical description of the system. The radial basis extends over a range of 400 a.u. and is divided into 80 finite elements. Each finite element contains 15 DVR basis functions. The maximal azimuthal quantum number of the angular basis is $l_{max} = 2$, while all angular basis functions have a magnetic quantum number of $m = 0$. The calculations were carried out on the ice2-queue of the Norddeutscher Verbund für Hoch- und Höchstleistungsrechnen (HLRN). To examine the weak scaling behavior, we chose the number of processors as $P = n^2 = M^2$.

Image 5.1 shows the weak scaling behavior of the algorithm, with and without the ESP scheme, in comparison to the ideal behavior. We can observe that the scaling behavior of our parallelization scheme is by no means ideal, even if we see a reasonable amount of speedup. It is evident that application of the ESP scheme during the propagation, changes the scaling behavior of the MCTDHF scheme. To understand this, we look at the serial fraction of the algorithm, which was calculated with the Karp-Flatt metric (5.4). The serial fraction is shown in figure 5.2 as a function of the number of processors. We observe that the serial

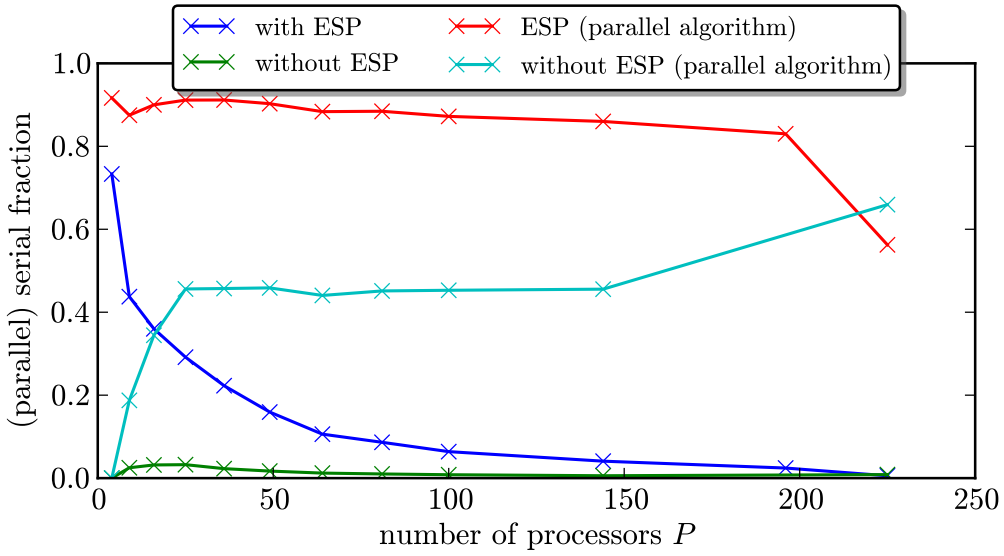

Figure 5.2: (Parallel) serial fraction of the (parallel) algorithm in dependency of the number of processors for the test system. All quantities were computed from the speedups shown in figure 5.1.

fraction is almost zero, if we do not apply the ESP scheme, but starts at a larger value otherwise. This explains the inferior results, when using the ESP scheme in addition to the parallelization, as we spend more time in a non-parallelized portion of the algorithm. The decay of the serial fraction can be explained if we compare the asymptotical runtime of the ESP scheme with the asymptotical runtime of the parallelized portion. The calculation of the two-particle quantities lies in $O(M^2)$, whereas the EPS scheme lies in $O(M)$. Hence, the ration between the time spent in the serial EPS algorithm and the time spent on the parallel calculation of two particle quantities drops with the number of orbitals M, and thereby with the number of processors P. This also explains the huge jump in the speedup for a large number of processors which we see in figure 5.1. Another feature of the algorithm is depicted in figure 5.2. We note that the serial fraction of the parallel algorithm—which was obtained using Eq. (5.3) and denoted as the parallel serial fraction—is roughly constant, even if the ESP scheme is not applied. The difference between the parallel serial fraction and the serial fraction is that the parallel serial fraction is calculated from an actual parallel run of the program, while the serial fraction is calculated with regard to a serial run. This shows us that the poor scaling in this case is caused by the remaining serial portions of the algorithm, which are identical to the calculation of the single-particle contributions. If we would parallelize these parts, we should observe a significant enhancement of

the scaling behavior.

5.5 Summary

In the previous section, we have observed that we have successfully parallelized the MCTDHF program. While the obtained speedups are by no means optimal, due to the mentioned reasons, it is a success from a practical point of view. Due to the reduced runtime, we were able to treat much more complex system with increased accuracy. We hope to circumvent the causes of the mentioned shortcomings in the future by using a more elaborate parallelization scheme.

6 The experiment

In this chapter, we will characterize the computer experiment which we will perform later by using the MCTDHF method. First, we will discuss the choice of beryllium as a test system and then give a description of several possible photo-ionization processes at the example of this atom. In the last part of the chapter, we will introduce the pump-probe scheme and detail the measurement procedures.

6.1 The system and processes

We have chosen beryllium as our test system, as it is the first atom with more than two electrons, in which all energy level are fully occupied making the theoretical description much easier. Since it has four electrons, much more complex and interesting processes can occur as compared to for example helium. As we have to simulate four electrons, the numerical effort is increased by orders of magnitude with regard to smaller systems. In addition, we need a large radial extension and a very accurate grid to describe the photo-ionization processes, which we want to simulate in the following, correctly. To our best knowledge, we are one of the first groups, which have simulated beryllium with all four electrons, while previous calculations have either frozen the core or the valence electrons [8, 9]. The only other work in this direction, which we have found during this work, was done by Saha and Caldwell [11]. Before we will discuss several possible processes, we should note that we cannot describe these processes using single-particle orbitals, as these are meaningless in the correlated case due to the use of more than one Slater determinant to represent the state. Nevertheless, we will use this primitive single-particle picture as a simple model to describe these processes qualitatively, as the description in the many-particle picture is very tedious and not intuitive. It is also a common convention to label many-particles states with the leading configuration.

The simplest photo-ionization process is the so called direct ionization, during which an electron is brought into the continuum by absorbing a single photon without the involvement of other electrons in the process. Since only one electron is active during the process, it is even included in the Hartree-Fock approximation. The first process, which we will discuss and which requires correlations, is the shake-up ionization. During a shake-up two electron absorb a single photon, which is only possible due to the correlations between the two particles, and one of them

is ionized. The other electron is excited to another bound state. Since the two electrons share the energy of the photon, the kinetic energy of the ionized photon must be lower with regard to the direct ionization process with the same photon energy due to energy conservation, which can be measured during an experiment. The energy difference between an ionized electron which originates from the direct ionization process and the electron which was ionized during the shake-up process is equal to the excitation energy of the other electron. A process which is conceptional similar to the shake-up process is the one-photon double ionization. Again, two electrons absorb a single photon on account of the correlations. The only difference to the shake-up process is that the energy of the photon is large enough to ionize both electrons. Hence, one could view this process as a special case of the shake-up process, in which the excited state is a continuum state. The last process, which we will discuss now, is the Auger decay. Before the Auger decay occurs, a core electron is ionized, for example by direct ionization, which leaves a hole at its former position. Due to correlations between the remaining electrons, a state with a higher energy can decay after a certain time and the electron, which has occupied this state, fills the core hole. Since the new core electron has now a lower energy, the excess energy has to be redistributed to other parts of the system. One possible outcome of this redistribution is that another electron is ionized by using the excess energy. Figure 6.1 also depicts these processes graphically in the single particle picture. From all these processes we have chosen the investigation the shake-up process in detail, since it is the easiest process, which involves correlations. The big obstacle, which discourages us from investigation of the one-photon double ionization or the Auger decay, which would be also appealing, is the fact that these processes emit two electrons into the continuum. As we will see later, the representation of a decent two-particle continuum is a quite tough task. Hence, the shake-up process is more appealing as a first test case.

Since we want to generate time-resolved results, we need a method to create these. One possibility is the pump-probe scheme. During the application of this scheme the system is excited by using a laser pulse, the so called pump pulse. If the system was previously in the ground state, this essentially starts a non-trivial time evolution and defines a reference time. Afterwards the excited system is exposed to a second pulse, the probe pulse, after a certain time delay τ. The only purpose of the probe pulse is to project the occupation of all energy levels within the atom into the continuum where we can measure it. The theoretical justification for this scheme is Fermi's golden rule, which qualitatively states in this case that the occupation of the final continuum state is proportional to the occupation of the initial state, if a weak electro-magnetic dipole field is used for the excitation. Fermi's golden rule also states that the energy difference is proportional to the frequency of the pump pulse. Hence, we can calculate the energy of the atomic energy level by measuring the energy of the continuum electron. By performing this experiment

repeatedly for different time delays τ, we can probe the occupation within the atom at different time points, which should differ due to the previous excitation. If we append all these measurements in chronological order, we effectively get a movie about the time evolution of the occupation within the atom.

The figures 6.1 and 6.2 illustrate the pump-probe scheme in the single-particle picture for the example of beryllium. A photon with the energy ω is absorbed by the $2s$ electrons, which are either brought into the continuum by direct ionization or shake-up ionization. To describe the shake-up in this model, we need to assume that two independent electron can absorb a single photon. This is normally only possible if both electrons are correlated. During the shake-up process, the other $2s$ electron is excited to the $3p$ level in this example, which lies above the $2s$ level by an energy ΔE. The energy of the ionized electron is reduced by this energy, which results in the energy difference ΔE with regard to the direct ionization process. After one of the $2s$ electrons is either ionized by direct ionization or by shake-up ionization, the probe pulse hits the system after a certain time. During the shake-up process the other $2s$ electron was excited to the $3p$ level. The probe pulse can now ionize the new $3p$ electron by direct ionization. Since the $3p$ level lies above the $2s$ level by an energy of ΔE, one observes the ionized electron with an about ΔE higher kinetic energy. This results in an energy spectrum with three peaks, which are displaced by the energy difference ΔE. During this work, we have used pulses of the form

$$\boldsymbol{E}(t) := \boldsymbol{E}_0 \sin(\omega t) \begin{cases} \sin\left(\pi \frac{t-t_0}{\sigma}\right)^2 & t \in [0, \sigma] \\ 0 & \text{otherwise} \end{cases} . \tag{6.1}$$

The peak intensity I_0 from which the amplitude E_0 is calculated is fixed to $10^{13}\ \frac{\mathrm{W}}{\mathrm{cm}^2}$.

6.2 Quantities and measurement procedures

After we have introduces the pump-probe scheme, we will now detail the examined quantities and the necessary measurement procedures.

One quantity, in which we are interested, is the single-ionization yield. Effectively, the single-ionization yield is the probability that we observe at least one electron outside of the atom. The outer zone of the atom is defined by a previously specified ionization radius R. This leads to the formal definition of the single-ionization yield operator

$$\hat{I}_1 := \int_R^\infty \mathrm{d}r\ |r\rangle\langle r| \,, \tag{6.2}$$

which is essentially the projector onto the exterior of the atomic system. The $\{|r\rangle\}$ are the eigenstates of the radial part of the position operator. In a similar manner,

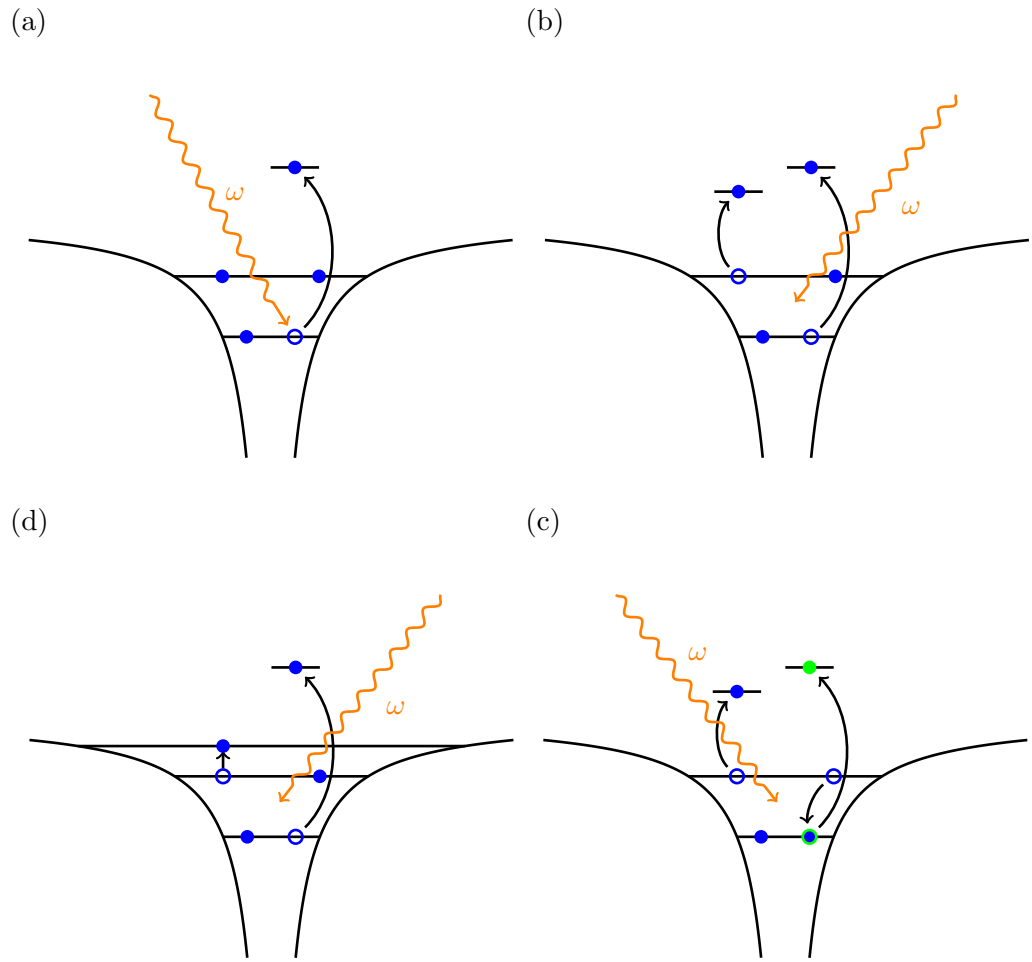

Figure 6.1: Illustrations of several ionization processes, which are possible for beryllium, in the single-particle picture. The processes depicted here are the direct ionization (a), the one-photon double ionization (b), the shake-up ionization (c) and the auger decay (d).

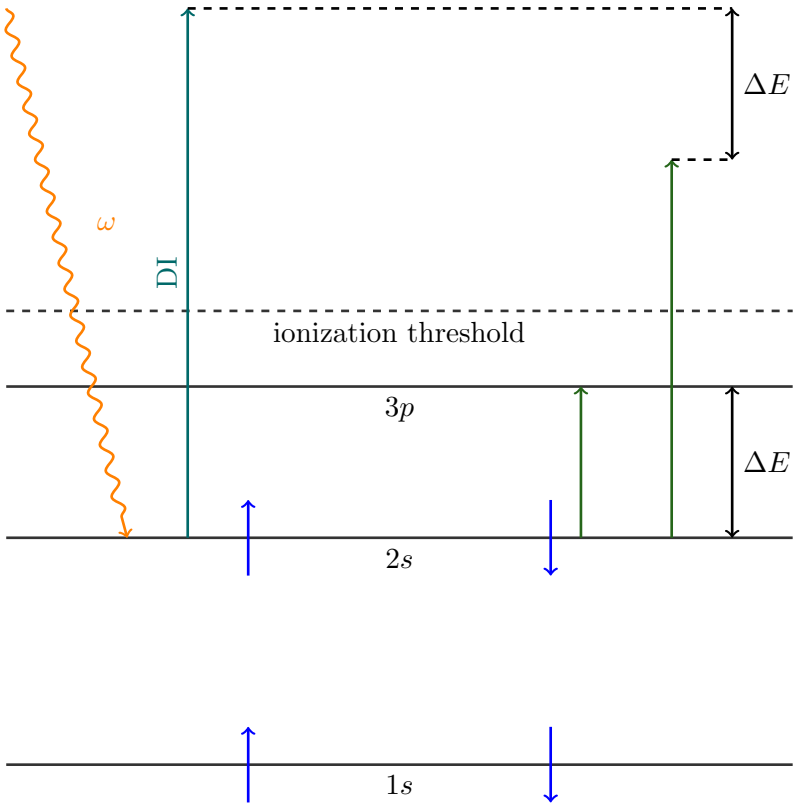

Figure 6.2: A beryllium atom during the pump pulse in the single-particle picture. The direct ionization and the shake-up ionization (green) are depicted as possible processes.

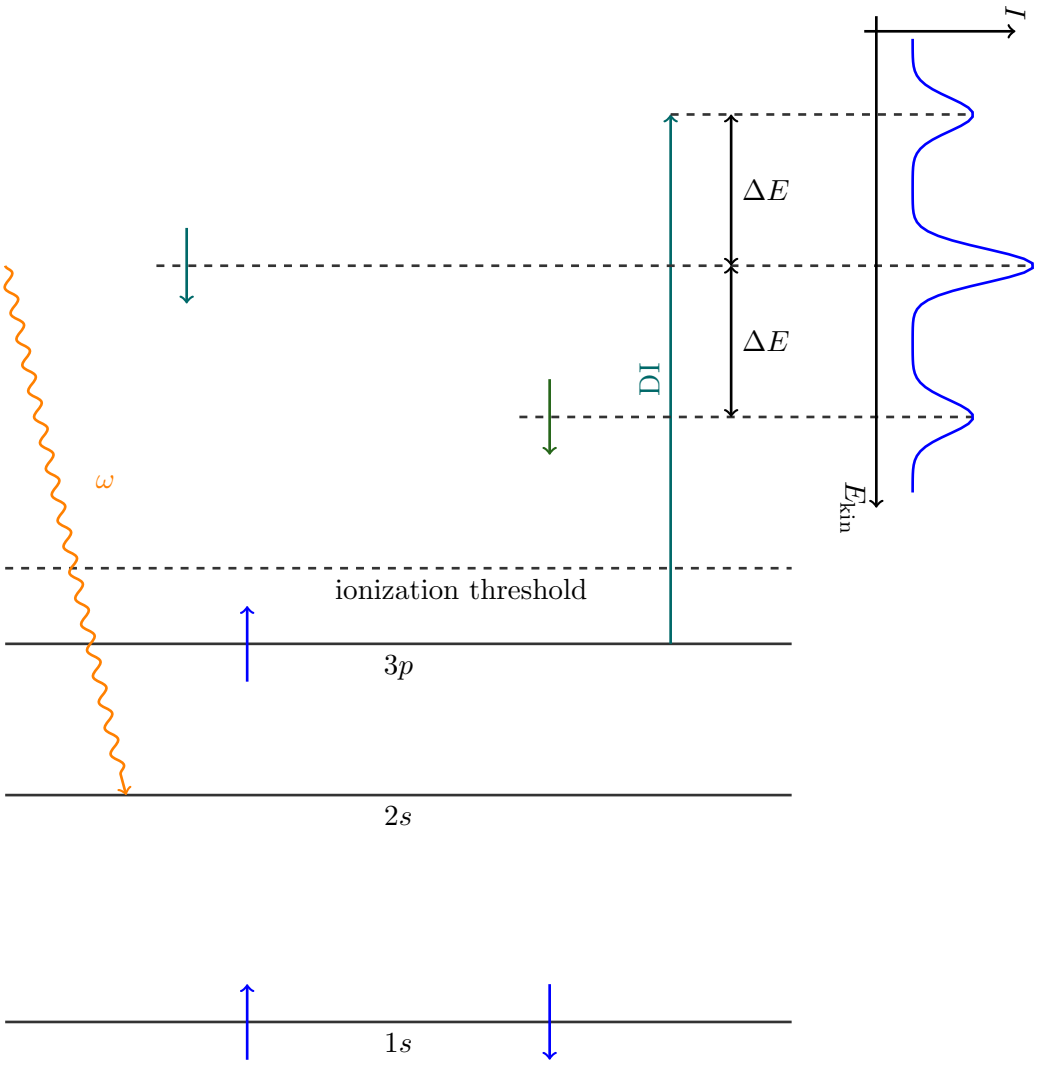

Figure 6.3: A beryllium atom during the probe pulse in the single-particle picture, after a $2s$ electron is either ionized by direct ionization or by shake-up ionization (green). The graph in the top right corner depicts the resulting energy spectrum.

one can define the operator for the double-ionization yield

$$\hat{I}_2 := \int_R^\infty \mathrm{d}r \int_R^\infty \mathrm{d}r' \; |r\rangle \left|r'\right\rangle \left\langle r'\right| \langle r| \,, \tag{6.3}$$

which measures the probability to observe at least two electrons in the exterior of the atom. Care must be taken if one uses this definition, since the product structure of these projectors implies that the electrons must be neither correlated with the ion, nor with any other ionized electron. If this is a valid assumption is the topic of ongoing discussions within the community [30–32]. After we have defined these operators, we can calculated their expectation values using the second quantization formalism, introduced in section 2.3.2.

The other quantity, which we will use below, is the kinetic energy density, which is defined as the probability (density) with which a certain kinetic energy is occupied by an electron. Since we are only interested in electrons within the exterior of the atom, we apply the projector (6.2) to the many-particle state and calculate the expectation value of the projectors onto the momentum eigenstates $|p\rangle\langle p|$. This leads to the momentum density

$$\rho(p) := \langle\Psi| \hat{I}_1 \, |p\rangle\langle p| \, \hat{I}_1 \, |\Psi\rangle \tag{6.4}$$

for a state $|\Psi\rangle$. Afterwards we can use the energy dispersion relation of a free particle,

$$E_{\mathrm{kin}} = \frac{p^2}{2}, \tag{6.5}$$

under the assumption that the particle is indeed free to perform a variable transformation and obtain the kinetic energy spectrum. The validity of the assumption is guaranteed by the projector $\hat{I}_1$, if we have chosen a proper ionization radius R. During this work, we have used an ionization radius of $R = 40$ a.u., which seems to give consistent results. Again, this quantity is only meaningful if there are no correlations between the ionized electron and the ion.

7 Numerical results

In this chapter, we will discuss the numerical results which were obtained by using the MCTDHF scheme. In the first part, we will investigate the ground state of beryllium and the convergence behavior of the MCTDHF calculations with regard to the angular basis. Afterwards, we will the properties of the photo-ionization processes based in the pump-probe spectrum and the ionization yield which were obtained from time-dependent calculations. In the last part, we will examine the spatial structure of the emitted density.

7.1 The beryllium ground state

As a first test, we will calculate the ground state energy of beryllium for different numbers of orbitals M. Since the bound density is contained in a small region by the Coulomb potential, we can afford to use a small radial grid of 30 atomic units for these calculations. The radial dimension is divided into 10 elements, each containing 20 FEDVR basis functions. The number of angular basis functions is adjusted to assure the convergence of the results. These are summarized in table 7.1. In addition the amount of correlation, which is covered by the MCTDHF approximation, with regard to the exact ground state energy of $E_0^{\text{exact}} = -14.667$ Ha [33] was calculated. We observe that the amount of correlations rises rapidly in the range $M \in [2, 7]$. After $M = 7$, the convergence slows down, and after $M = 10$ the amount of correlation reaches a value of roughly 90 % and is almost constant. This behavior can be easily deduced from figure 7.1. The rapid increase of the covered correlations is an indicator that the MCTDHF method is able to accurately describe the ground state including correlation effects using only a small number of orbitals, and therefore Slater determinants. If we would have used CI instead, we would have needed to perform calculations with several thousand orbitals and a corresponding number of Slater determinants, which would have made the simulations much more challenging.

Another important observation is that we need to gradually increase the angular basis set to ensure the convergence of the results. This indicates that the angular structure of the ground state gets much more complex through the correlations in comparison to the Hartree-Fock ground state. This also means that we will need much more computational resources for a larger number of orbitals. Due to the need for such a large single-particle basis, the performance improvements

$l_{\max}$	$m_{\max}$	M	E_0[eV]	correlations (%)
2	1	2	−14.573	0
		3	−14.587	15
		4	−14.605	34
		5	−14.612	41
		6	−14.619	49
		7	−14.634	65
3	2	8	−14.646	78
		9	−14.653	85
		10	−14.655	87
		11	−14.656	88
		12	−14.657	89
		13	−14.657	89
4	3	14	−14.658	90
		15	−14.658	90
		16	−14.659	91

Table 7.1: Ground state energy of beryllium and the amount of covered correlations for different numbers of orbitals M. The maximal azimuthal quantum number and the maximal magnetic quantum number are adjusted to assure the convergence of the energy if necessary.

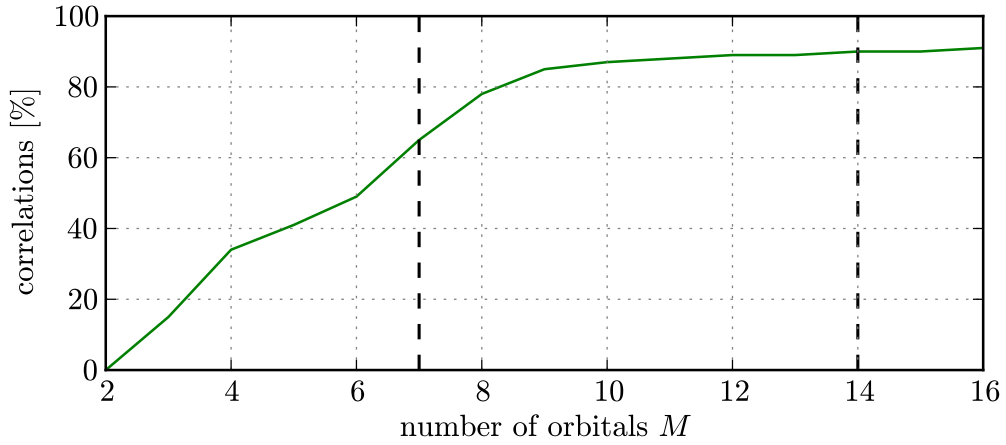

Figure 7.1: Percentage of the correlations which is covered by the MCTDHF approximation with regard to the exact ground state energy. The dashed lines mark the numbers of orbitals at which the angular basis is enlarged.

during this work become essential, since we could not perform these calculations otherwise. Especially, the stiffness reduction is important as the integration would be seriously impaired without it for these basis sets.

7.2 Convergence regarding the angular basis

To estimate the impact of the need for an increased basis if one uses a larger number of orbitals onto the photo-ionization, we investigate the relative error of the single-ionization yield with respect to the most accurate result in dependence of the size of the angular basis. As a test system we use beryllium with a radial extent of 200 a.u.. The radial dimension is divided into 64 elements with 20 basis functions in the first three elements and 10 basis functions otherwise. From our experience, these are enough basis functions to obtain accurate results. The parameters for the electric field are most likely not relevant in this case, since we are only interested in the qualitative behavior.

In the case of Hartree-Fock, which is depicted in figure 7.2, one obtains the expected results. If we only use a single angular basis function with quantum numbers $l = 0$ and $m = 0$, we get a relative error of one, as the result would already be wrong in the case of an ideal atom due to the occurrence of a p - electron in the continuum. For all other cases the error essentially vanishes, which means that the state in Hartree-Fock approximation is almost radial symmetric and a single additional angular basis function with $l = 1$ is sufficient to describe the system

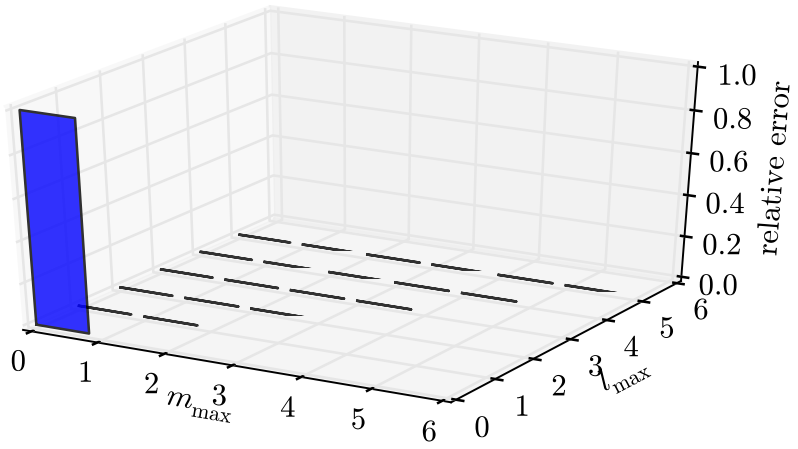

Figure 7.2: Dependency of the relative error of the single-ionization yield on the size of the angular basis for Hartee-Fock. The reference value is the most accurate value, i.e., the value for the largest angular basis.

accurately.

If we proceed to a simulation of the same system with seven orbitals and compare the error bars in figure 7.3 with those for Hartree-Fock, the results do not look as promising anymore. In contrast to the Hartree-Fock results, the error does not vanish for a set of only two angular basis functions, but we need to increase the maximal azimuthal quantum number and the maximal magnetic quantum number at the same time, which is consistent with our results from the ground state calculations and therefore not that bad. Unfortunately, the error increases for example at the position $m_{\max} = 3$ and $l_{\max} = 4$ and decreases again for a larger basis, which means that the convergence with regard to the angular basis is not monotone. This has far-reaching consequences, since a monotonic behavior would allow us to safely truncate the basis expansion once the error is sufficiently small. But in the case of a non-monotonic behavior we cannot do this without the danger that the error has another peak for an even larger basis.

One possibility to solve this problem would be to use another angular basis, for example an angular DVR basis, which might converge monotonically. Another origin of this error might be the length gauge, as the gauge can influence the convergence behavior of the basis. If this would be true, one could try to use another gauge, e.g., the velocity gauge, to circumvent the problem.

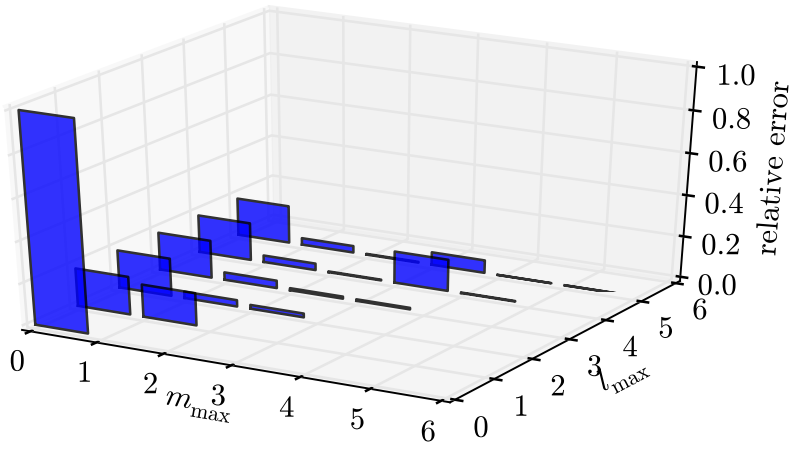

Figure 7.3: Dependency of the relative error of the single-ionization yield on the size of the angular basis for $M = 7$. The reference value is the most accurate value, i.e., the value for the largest angular basis.

7.3 Pump-Probe spectrum

After we have investigated the convergence of the solution in the last section, we will get to the time-resolved investigation of the shake-up process in beryllium. For that, we have used a radial FEDVR grid with an extent of 500 a.u., which is divided into 160 elements. Again, 20 basis functions are used for the first three elements. All other elements are constructed from 13 basis functions. The maximal azimuthal quantum number was 3 and the maximal magnetic quantum number was 1. A pulse with a frequency of 200 eV and a duration of 2.4 fs is used to excite the beryllium atom.

From the graphically depicted spectrum in figure 7.4, we can deduce that Hartree-Fock is able to successfully describe the direct ionization processes almost exactly, as can be seen from the comparison with the exact lines from the NIST database [34]. Only the energy of the $1s2s^2$ state is a little bit off, which can be explained by missing contributions to the correlation energy. If we increase the number of time-dependent orbitals to 6, the spectrum gains an additional feature in the form of another peak at the left slope of the $1s^22s$ direct ionization peak. By comparing the energy value with the exact spectrum from the NIST database, we can identify this peak as a result from the shake-up of the ion to the $1s^22p$ state. As expected, this process cannot be described by Hartree-Fock as it requires

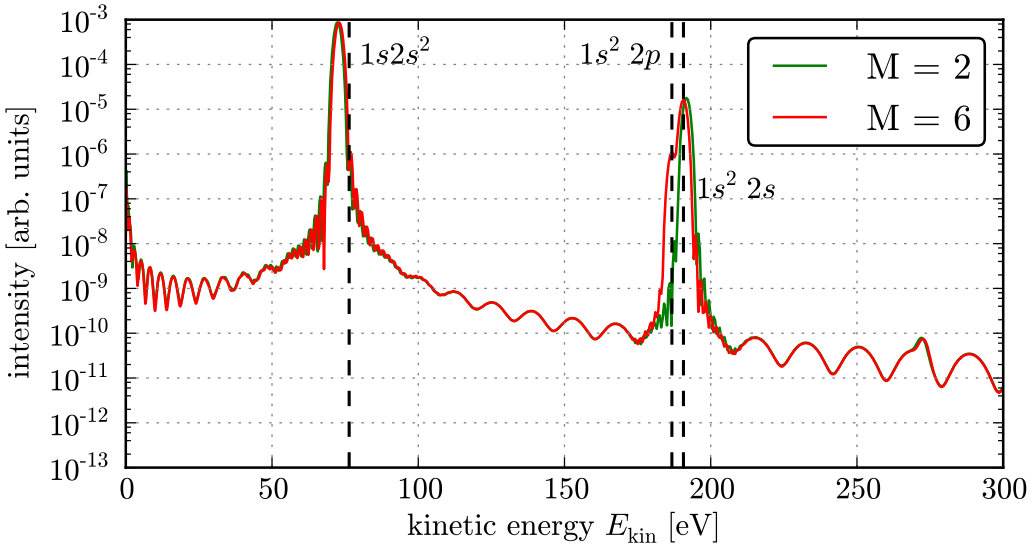

Figure 7.4: Kinetic energy spectrum of the continuum electron after the pump pulse for different MCTDHF approximations. The dashed lines mark the exact values of some spectral lines, which are taken from the NIST database [34].

correlations. Even as a stand-alone result, this is quite impressing, as we were able to simulate a correlated process with only a few time-dependent orbitals, which again shows the benefits of MCTDHF.

After the system was excited during the pump pulse, we expose the system to a probe pulse after a delay of 1.2 fs. The pulse was untuned, using an energy of 250 eV, to avoid an interference with the pump pulse. To counteract the increased propagation time of 3.6 fs, we enlarge the grid to 700 a.u. with 220 elements. This essentially duplicates the pump spectrum, except for a displacement of 50 eV due to the untuned second pulse, as can be seen from figure 7.5 for $M = 6$. What we would not have expected is that the structure is exactly reproduced, since an additional peak should occur at the other side of the $2s$ direct ionization peak due to the previous excitation of one $2s$ electron, as explained in section 6.1. From further investigations, which we have done during this work, we have deduced that this seems to be caused by a poor description of the two-particle continuum, as the representation of correlations seems to be very good. This is indicated by the successful simulation of the shake-up process during the pump pulse. This effect might be caused by the low occupation of the continuum states in comparison to the bound states of the atom. It is reasonable that the MCTDHF algorithm might discard these small contributions in favor of a good description of the bound states.

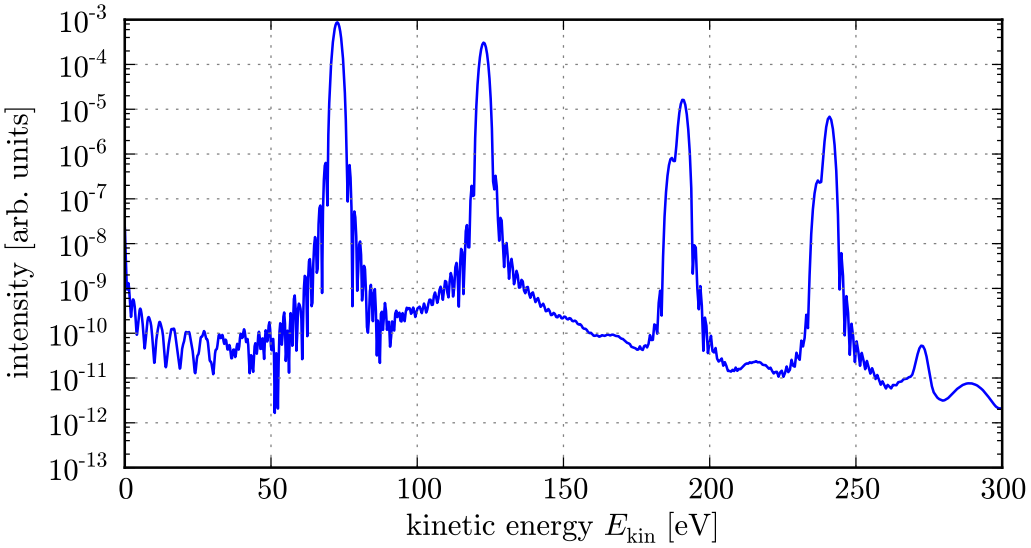

Figure 7.5: Kinetic energy spectrum of the continuum electrons after the probe pulse for $M = 6$. Before, the system was excited by a pump pulse with a delay of 1.2 fs between both pulses.

It is also plausible, why the single-particle continuum is not effected that much, as the structure of the two-electron continuum is much more complex. In theory, we might not observe the additional peak, because the delay was too short for the process to occur, but this is highly unlikely as the time range of 1.2 fs is much larger than the usual process time of similar processes.

7.4 Ionization yields

To verify the assumption that the two-electron continuum is not represented well, we will compare the single-ionization yield with the double-ionization yield, since previous calculations for helium [10] have shown that a similar problem occurs for the double-ionization yield. To perform the calculations, we have used a radial grid with an extension of 400 a.u., that is divided into 128 elements. Again, the number of basis functions within the first three elements is 20. A number of 10 basis functions is used to construct all other elements. The maximal azimuthal quantum number was 4 and the maximal magnetic quantum number was 3. The system was excited by a pulse with varying frequencies and a fixed duration of 2.4 fs.

The single-ionization yield, shown in figure 7.6, exhibits the expected qualitative

behavior. For low photon energies in the range from 50 eV to 100 eV, only the $2s$ electrons are ionized, since the photon energy is too low to allow an ionization of the core electrons, and the single-ionization yield decreases monotonically. The decrease is easily explained by the consideration that the binding energy of the $2s$ electrons becomes neglectable for large photon energies. This means, that the photon is essentially a free particle and a free particle cannot absorb a photon, since this would either violate the conservation of energy or the conservation of momentum. Therefore, it is less likely that an electron is ionized. At approximately 117 eV, a resonance occurs, i.e., two different processes interfere constructively. After a comparison with the atomic spectrum in the NIST database [34] we have identified this resonance, as an interference effect between the direct ionization of an $2s$ electron and the excitation of the atom to the $1s2s^22p$ state. This effect is even slightly reproduced by the Hartree-Fock approximation, since both interfering processes do not require correlations, even so the effect is underestimated by the mean-field approximation. At 123.35 eV we reach the ionization threshold for the $1s$ electrons and shortly after that the single-ionization yield rapidly increases. That the increase does not occur directly after we passed the threshold is caused by the portion of the correlation energy which is not included into this MCTDHF approximation. As one can observe, the simulation with $M = 6$ shifts the occurrence of this increase into the correct direction, and one would expect that this trend is continued for larger numbers of orbitals until the position of the threshold is reached.

While the behavior of the single-ionization yield is sensible, the behavior of the double-ionization yield, depicted in figure 7.7, is not, as it shows essentially the same behavior. This seems to be wrong, as one would expect an increase of the double-ionization yield with higher photon energies due to a larger number of possibilities to ionize two electrons. We would expect that the behavior of both ionization yields is essentially identical for Hartree-Fock, since the double-ionization yield is proportional to the single-ionization yield squared. This is caused by the ansatz of the Hartree-Fock state as an anti-symmetrized tensor product. As the $M = 6$ MCTDHF approximation behaves in a similar manner, we deduce that this is also caused by the product ansatz of the configurations. It seems that the few determiants which are used to represent the many-particle state are not sufficient to overcome this structure within the continuum. This is most likely the root cause of the insufficient two-electron continuum. Since we used an even larger angular basis, this does not seem to be an issue.

The identification of this important problem is one of the major results of this work, since it inhibits the simulation of any two-particle ionization processes, if it is not solved. This includes important methods for time-resolved measurements, like pump-probe or streaking, and many interesting, and commonly investigated, processes, like Auger decay and one-photon double ionization. To overcome this

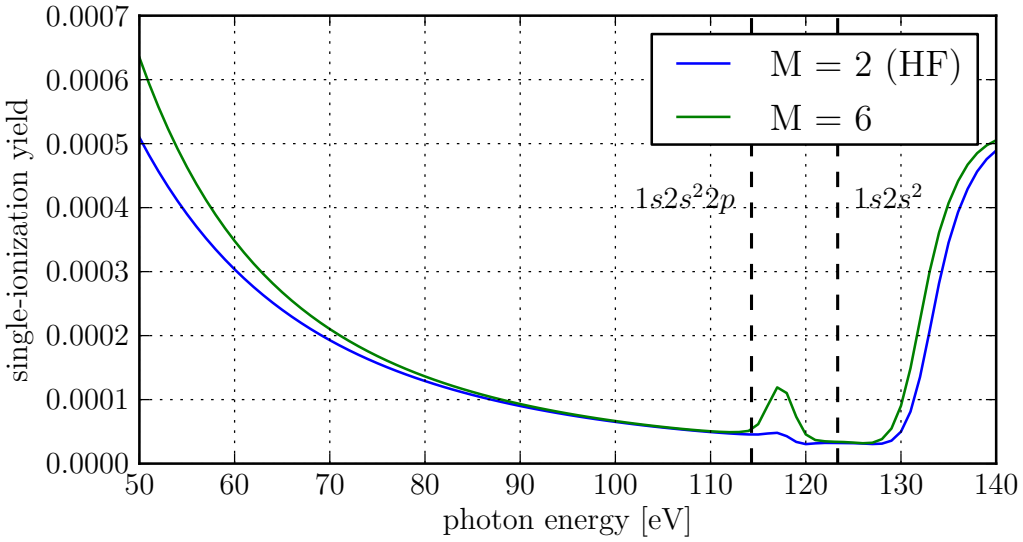

Figure 7.6: Single-ionization yield of beryllium for different MCTDHF approximations. The dashed black lines mark the positions of the resonance and the $2s$ ionization threshold, which were extracted from the NIST database [34].

problem seems to be a rather complicated task, since we have tried several promising schemes during this work to solve or at least circumvent this problem without any success. For example, one ansatz was to deduce the time-dependency of the occupations directly from the ion [35], which fails as the decomposition of the time-dependent state into two non-correlated systems is not unique, even if the correlations between the two systems have vanished during the ionization process. Similar theoretical or practical problems inhibit the use of other schemes. While there are other methods which we want to investigate in the future, these are very complicated and would go beyond the scope of this work. We will give a brief description of these methods in chapter 8.

7.5 Spatial structure of the emitted density

As we have already observed that the angular structure gets more complicated for an increasing number of orbitals, it would be interesting to investigate this changed structure. This can be done by examining the density of the emitted electrons. We have done this for a radial grid with an extent of 200 a.u. that is divided into 64 elements with the already used configuration of 20 basis functions within the first

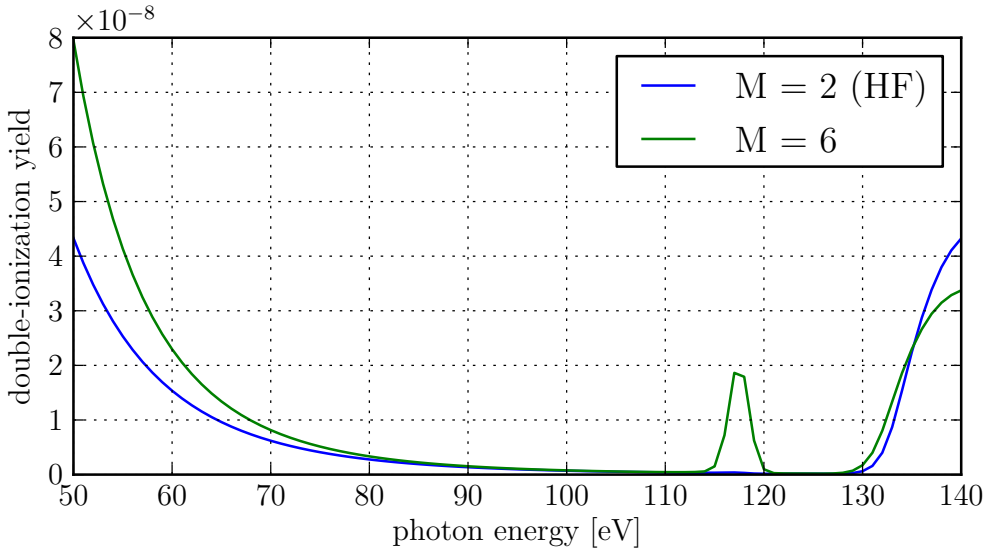

Figure 7.7: Double ionization of beryllium for different MCTDHF approximations.

three elements and 10 in all others. The maximal azimuthal quantum number was 3 and the maximal magnetic quantum number was 2. The system was excited by a pulse with a frequency of 50 eV and a duration of 2.4 fs. Therefore, we can only ionize the $2s$ electrons.

The isosurfaces of the single-particle density for a value of 10^{-10} for Hartree-Fock and $M = 6$ are shown in figure 7.8. On can observe that the Hartree-Fock density has a rotational symmetry with regard to the z-axis, if one would rotate the plot. This is already known for the ideal system. At the same time, the density for $M = 6$ has no rotational symmetry, as we have expected from our previous observations, but is contorted within the direction of the x-axis into a bean-like shape. No density is emitted within the x-y plane since we use a pulse, which is linearly polarized in z-direction, and therefore does not act in this direction.

A possible explanation for this effect is that particles that are not emitted directly into the z-direction receive an attractive force from the core, which can be modeled as an additional core charge. In this case their classical trajectories might be modified in such a way that the particles enter the previously forbidden region. We have done simulations which use this model and depicted them graphically in figure 7.9. As we can see, the Hartree-Fock results of the modified system match the contour lines of the $M = 6$ results almost exactly for the direction which deviate heavily from the z-axis, while the results within this direction are described very well by the original Hartree-Fock calculations, which indicates an angular dependency of this effect. The additional charge could be generated by

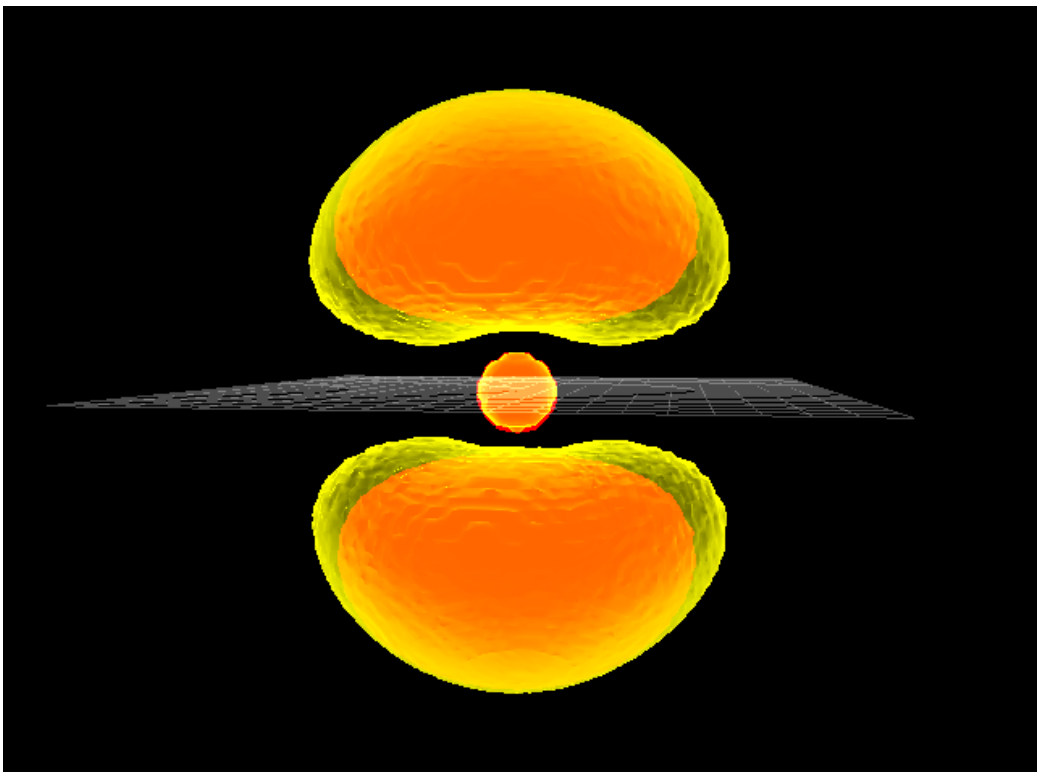

Figure 7.8: Isosurfaces of the single-particle density for a value of 10^{-10} for an excited beryllium system. for Hartree-Fock (red) and $M = 6$ (yellow).

a polarization of the atomic density due to correlations, which is sensible as the correlation energy of the $2s$ electrons is comparable to the energy difference of the $2s$ level to its excited states [36]. This assumption is also consistent with the results for the ionization of the $1s$ electrons by using a pulse of frequency 150 eV in figure 7.10. In this case, Hartree-Fock is almost exact, as there are no excited states within the order of magnitude of the correlation energy with respect to the $1s$ level. In neither case, Hartree-Fock can describe this effect, as the emitted electron always sees a neutral system due to the screening of the core by the mean-field in this case. While we have given a preliminary explanation of this effect, we should further investigate and verify this interesting effect in the future.

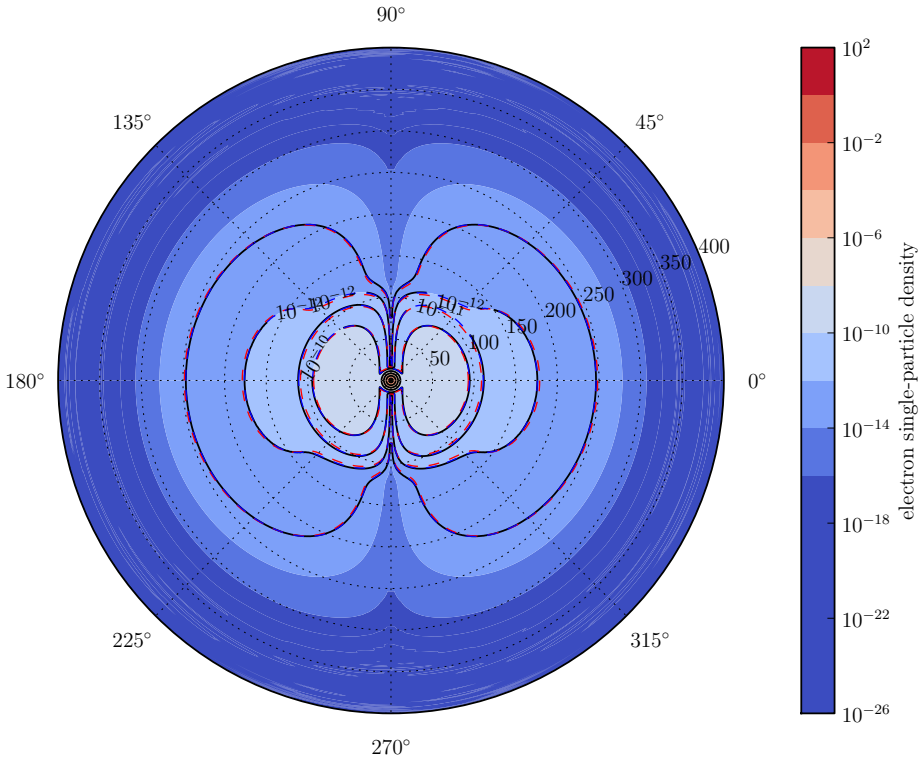

Figure 7.9: A cut through the single-particle density within the x-z plane after the $2s$ level was ionized by a laser pulse for $M = 6$ (color values and black contour lines). The dashed red contour lines denote the results for Hartree-Fock. The dashed blue lines denote the results for Hartree-Fock and an additional core charge of 0.7.

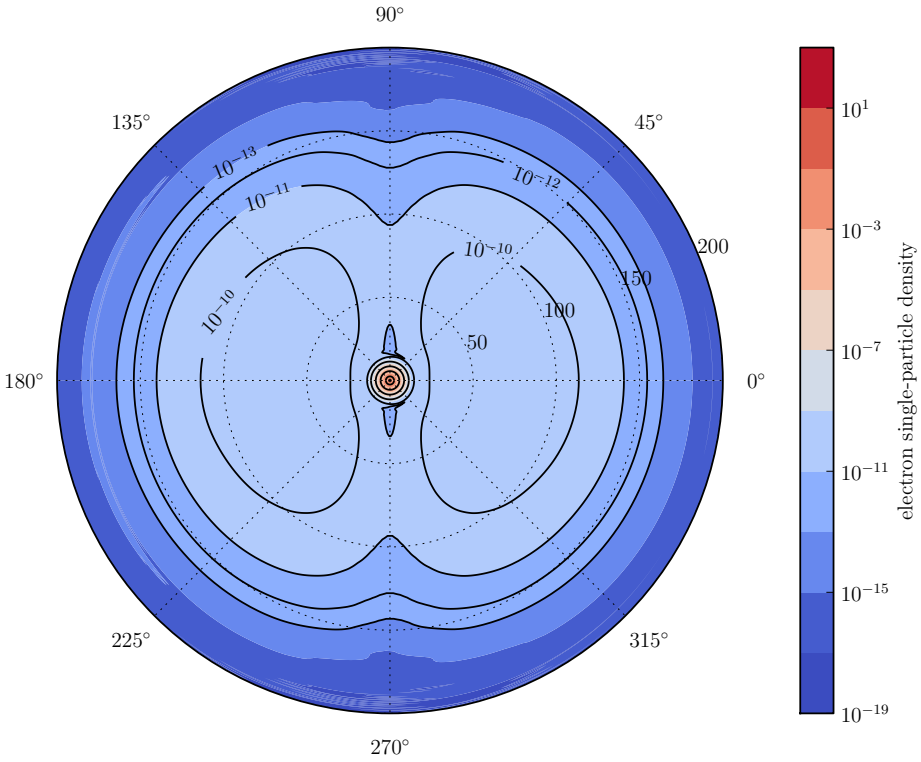

Figure 7.10: A cut through the single-particle density within the x-z plane after the $1s$ level was ionized by a laser pulse for $M = 6$ (color values and black contour lines). The dashed red contour lines denote the results for Hartree-Fock. The dashed blue lines denote the results for Hartree-Fock and an additional core charge of 0.7.

8 Conclusions and outlook

To conclude this work, we summarize the experiences and results which we gained during this time. In the last part of this chapter, we will give a brief discussion of the consequences of this work and possible future directions in which we may continue.

In the first part of the work, we discussed the quantum theory of many-particle systems to create a theoretical foundation for the numerical methods, which are used in this work. We have started with the general mathematical structure of quantum mechanics, before we introduced the first representation of many-particle theory in the form of the first quantization and introduced important concepts of many-particle quantum mechanics. Since the first quantization is very tedious to use for the description of complex many-particle systems, we have introduced the second quantization as an alternative approach to many-particle systems. This gives us the building block to establish numerical methods for the numerical solution of the time-dependent many-particle Schrödinger equation. First we have discussed the historical methods of Configuration interaction and Hartree-Fock and discussed their advantages and shortcomings. With this knowledge as a starting point, we have motivated and introduced the idea of Multiconfigurational time-dependent Hartree-Fock. Afterwards we have deduced the equations of motion from a first principle, before we have closed this matter with a discussion of the chosen single-particle basis set and the implementation. Most notably, we were able to significantly improve the capabilities of our implementation during this work.

One of these improvements was the development of a solution for the problem of the so called stiffness, which is an intrinsic property of the MCTDHF equations and prevents the use of very accurate basis sets. To overcome this problem, we have proposed a domain-specific scheme, which we call the Energy subspace projection (ESP) method. In addition, we outlined a possible implementation of this scheme, which was integrated into our MCTDHF implementation during this work. We were able to show that our scheme reduces the problem while staying cheap enough to be applicable, and therefore allows us to use significantly enlarged basis set to describe our problems. Another improvement was the implementation of a parallelization scheme for the right-hand side of the MCTDHF equations. After the scheme was implemented, we have systematically investigated its performance and recognized some minor flaws. Nevertheless, the performance is adequate for a first

implementation and we were able to speed up the algorithm considerably, which has allowed us to simulate much more complex systems. The current implementation and the gained experiences give us a solid foundation for future improvements. Together, all performance improvements produce a significant speedup within the range 30 to 10000 and have enabled the simulations in the first place.

After we have introduced our computer experiment, particularly the pump-probe scheme, we have discussed the results of our simulations. In the course of investing the dependency of the ground state energy on the level of approximations, we have found that MCTDHF is able to produce very accurate results with only a few time-dependent orbitals. In addition, we have noticed that we need to enlarge the angular basis for more sophisticated approximations to represent the more complex structure of the state. Due to this, we have investigated the error, which is introduced by the truncation of the angular basis, and have noticed that the angular basis might not be well-chosen, as it does not converge monotonically. Afterwards, we have applied the pump-probe scheme to beryllium to obtain a time-resolved observation of shake-up processes. As a very promising result, we observed a shake-up process during the application of the pump pulse, which means that we are able to use MCTDHF to describe such results, which would not be practically possible with Hartree-Fock or Configuration interaction. Unfortunately, we were not able to successfully perform a full pump-probe calculation, as MCTDHF does not seem to be able to simulate a second electron within the continuum. To find the root cause of this problem, we have compared the single- and the double-ionization yield. This has resulted in the insight that MCTDHF is not able to overcome the product structure of the ansatz, and is therefore not able to accurately describe a two-particle continuum. Also the last calculations, in which we have considered the spatial structure of the emitted density, have demonstrated a distinct correlation effect, that we need to investigate further.

To solve the problem with the structure of the many-particle state, one could apply one of several extensions of the MCTDHF scheme. One of these extensions is the multilayer MCTDH scheme [37], which can be used to construct the many-particle state not only from single-particle states but also from two-particle orbitals. This might improve the description of two-particle quantities. Another possibility, that we have outlined together with Dr. David Hochstuhl during this work, would be to apply constrains to the orbitals and force them into the proper subspace. A distinct future direction might be the application of the MCTDHF scheme to larger atoms. Two extensions which are interesting in this regard are the TD-RASSCF [38] and the TD-CASSCF [39], as they can significantly reduce the computational complexity for systems with a large number of particles. In addition, we plan to improve the parallelization of our implementation and to port it to GPUs.

Bibliography

[1] K. Tiedtke, A. Azima, N. von Bargen, L. Bittner, S. Bonfigt, S. Düsterer, B. Faatz, U. Frühling, M. Gensch, C. Gerth, N. Guerassimova, U. Hahn, T. Hans, M. Hesse, K. Honkavaar, U. Jastrow, P. Juranic, S. Kapitzki, B. Keitel, T. Kracht, M. Kuhlmann, W. B. Li, M. Martins, T. Núñez, E. Plönjes, H. Redlin, E. L. Saldin, E. A. Schneidmiller, J. R. Schneider, S. Schreiber, N. Stojanovic, F. Tavella, S. Toleikis, R. Treusch, H. Weigelt, M. Wellhöfer, H. Wabnitz, M. V. Yurkov, and J. Feldhaus, "The soft x-ray free-electron laser flash at desy: beamlines, diagnostics and end-stations," *New Journal of Physics*, vol. 11, no. 2, p. 023029, 2009.

[2] U. Frühling, M. Wieland, M. Gensch, T. Gebert, B. Schütte, M. Krikunova, R. Kalms, F. Budzyn, O. Grimm, J. Rossbach, E. Plönjes, and M. Drescher, "Single-shot terahertz field driven x-ray streak-camera," *Nature photonics*, vol. 3, pp. 523–528, 2009.

[3] J. Feldhaus, T. Möller, E. Saldin, E. Schneidmiller, and M. Yurkov, "Pump–probe experiments in the femtosecond regime, combining first and third harmonics of SASE FEL radiation," *Nuclear Instruments and Methods in Physics Research Section A: Accelerators, Spectrometers, Detectors and Associated Equipment*, vol. 507, no. 1–2, pp. 435 – 438, 2003. ¡ce:title¿Proceedings of the 24th International Free Electron Laser Conference and the 9th Users Workshop.¡/ce:title¿.

[4] G. Haran, W.-D. Sun, K. Wynne, and R. M. Hochstrasser, "Femtosecond far-infrared pump-probe spectroscopy: A new tool for studying low-frequency vibrational dynamics in molecular condensed phases," *Chemical Physics Letters*, vol. 274, no. 4, pp. 365 – 371, 1997.

[5] Uiberacker M., Uphues Th., Schultze M., Verhoef A. J., Yakovlev V., Kling M. F., Rauschenberger J., Kabachnik N. M., Schroder H., Lezius M., Kompa K. L., Muller H.-G., Vrakking M. J. J., Hendel S., Kleineberg U., Heinzmann U., Drescher M., and Krausz F., "Attosecond real-time observation of electron tunnelling in atoms," *Nature*, vol. 446, pp. 627–632, apr 2007. 10.1038/nature05648.

[6] S. X. Hu and L. A. Collins, "Attosecond pump probe: Exploring ultrafast electron motion inside an atom," *Phys. Rev. Lett.*, vol. 96, p. 073004, Feb 2006.

[7] B. Schütte, S. Bauch, U. Frühling, M. Wieland, M. Gensch, E. Plönjes, T. Gaumnitz, A. Azima, M. Bonitz, and M. Drescher, "Evidence for chirped auger-electron emission," *Phys. Rev. Lett.*, vol. 108, p. 253003, Jun 2012.

[8] S. Laulan and H. Bachau, "One- and two-photon double ionization of beryllium with ultrashort ultraviolet laser fields," *Phys. Rev. A*, vol. 69, p. 033408, Mar 2004.

[9] F. L. Yip, C. W. McCurdy, and T. N. Rescigno, "Double photoionization of excited lithium and beryllium," *Phys. Rev. A*, vol. 81, p. 063419, Jun 2010.

[10] D. Hochstuhl and M. Bonitz, "Two-photon ionization of helium studied with the multiconfigurational time-dependent hartree–fock method," *The Journal of Chemical Physics*, vol. 134, no. 8, p. 084106, 2011.

[11] H. P. Saha and C. D. Caldwell, "K -shell photoionization of beryllium," *Phys. Rev. A*, vol. 40, pp. 7020–7025, Dec 1989.

[12] S. Gustafson and I. Sigal, *Mathematical concepts of quantum mechanics*. Universitext - Springer-Verlag, Springer Berlin Heidelberg, 2011.

[13] A. Fetter and J. Walecka, *Quantum Theory of Many-particle Systems*. Dover books on physics, DOVER PUBN Incorporated, 2003.

[14] P. A. M. Dirac, "A new notation for quantum mechanics," *Mathematical Proceedings of the Cambridge Philosophical Society*, vol. 35, pp. 416–418, 7 1939.

[15] J. Gray, "The shaping of the riesz representation theorem: A chapter in the history of analysis," *Archive for History of Exact Sciences*, vol. 31, no. 2, pp. 127–187, 1984.

[16] C. W. Helstrom, "Quantum detection and estimation theory," *Journal of Statistical Physics*, vol. 1, no. 2, pp. 231–252, 1969.

[17] J. Jauch, *Foundations of quantum mechanics*. Addison-Wesley series in advanced physics, Addison-Wesley Pub. Co., 1968.

[18] M. Fierz, *Ueber die relativistische Theorie kräftefreier Teilchen mit beliebigem Spin*. Birkhäuser, 1939.

[19] W. Pauli, "The connection between spin and statistics," *Phys. Rev.*, vol. 58, pp. 716–722, Oct 1940.

[20] D. Hochstuhl, *Multiconfiguration methods for the numerical simulation of photoionization processes of many-electron atoms.* PhD thesis, Christian-Albrechts-Universität zu Kiel, 2013.

[21] O. E. Alon, A. I. Streltsov, and L. S. Cederbaum, "Unified view on multi-configurational time propagation for systems consisting of identical particles," *The Journal of Chemical Physics*, vol. 127, no. 15, p. 154103, 2007.

[22] W. H. Press, S. A. Teukolsky, W. T. Vetterling, and B. P. Flannery, *Numerical Recipes 3rd Edition: The Art of Scientific Computing.* New York, NY, USA: Cambridge University Press, 3 ed., 2007.

[23] The HDF Group, "Hierarchical data format version 5," 2000-2013.

[24] P. Gill, W. Murray, and M. Wright, *Practical optimization.* Academic Press, 1981.

[25] L. B. Rall, *Automatic Differentiation: Techniques and Applications*, vol. 120 of *Lecture Notes in Computer Science.* Berlin: Springer, 1981.

[26] M. Jerosolimski and L. Levacher, "A new method for fast calculation of jacobian matrices: automatic differentiation for power system simulation," in *Power Industry Computer Application Conference, 1993. Conference Proceedings*, pp. 411–417, 1993.

[27] G. M. Amdahl, "Validity of the single processor approach to achieving large scale computing capabilities," in *Proceedings of the April 18-20, 1967, spring joint computer conference*, pp. 483–485, ACM, 1967.

[28] J. L. Gustafson, "Reevaluating amdahl's law," *Commun. ACM*, vol. 31, pp. 532–533, 1988.

[29] A. H. Karp and H. P. Flatt, "Measuring parallel processor performance," *Commun. ACM*, vol. 33, pp. 539–543, May 1990.

[30] L. A. A. Nikolopoulos and P. Lambropoulos, "Multichannel theory of two-photon single and double ionization of helium," *Journal of Physics B: Atomic, Molecular and Optical Physics*, vol. 34, no. 4, p. 545, 2001.

[31] E. Foumouo, G. Lagmago˜kamta, G. Edah, and B. Piraux, "Theory of multi-photon single and double ionization of two-electron atomic systems driven by short-wavelength electric fields: An ab initio treatment," *Physical Review A (Atomic, Molecular, and Optical Physics)*, vol. 74, no. 6, pp. 063409+, 2006.

[32] R. Nepstad, T. Birkeland, and M. Førre, "Numerical study of two-photon ionization of helium using an *ab initio* numerical framework," *Phys. Rev. A*, vol. 81, p. 063402, Jun 2010.

[33] J. Komasa, W. Cencek, and J. Rychlewski, "Explicitly correlated gaussian functions in variational calculations: The ground state of the beryllium atom," *Phys. Rev. A*, vol. 52, pp. 4500–4507, Dec 1995.

[34] Y. Ralchenko, A. E. Kramida, J. Reader, and N. A. S. D. Team, "NIST Atomic Spectra Database (version 5.0)," 2012.

[35] Y. K.-E. Yasutaka Taniguchi, "Separation of a slater determinant wave function with a neck structure into spatially localized subsystems," *pre-print*, 2012. arXiv:1111.1759v2.

[36] H. P. Kelly, "Correlation effects in atoms," *Phys. Rev.*, vol. 131, pp. 684–699, Jul 1963.

[37] U. Manthe, "A multilayer multiconfigurational time-dependent hartree approach for quantum dynamics on general potential energy surfaces," *The Journal of Chemical Physics*, vol. 128, no. 16, p. 164116, 2008.

[38] L. B. M. Haruhide Miyagi, "Time-dependent restricted-active-space self-consistent field theory for laser-driven many-electron dynamics," *pre-print*, 2013. arXiv:1304.5904.

[39] K. L. I. Takeshi Sato, "Time-dependent complete-active-space self-consistent field method for multielectron dynamics in intense laser fields," *pre-print*, 2013. arXiv:1304.5835.

Danksagungen

Zunächst möchte ich meinem Betreuer, Herr Prof. Dr. Michael Bonitz, danken, der diese Arbeit erst ermöglicht hat und mir die Freiheit gab, dieses faszinierende Thema auf meine eigene Art und Weise zu erschließen. Besonders danken möchte ich ihm für die Möglichkeit das interessante Thema dieser Arbeit im Rahmen einer Promotion weiter zu erforschen. Des Weiteren möchte ich David Hochstuhl danken, der mir jederzeit mit Rat zur Seite stand und mich an seinem umfassenden Wissen über Quantentheorie hat Teilhaben lassen. Ein besonderer Dank geht an Sebastian Hermanns für das Korrekturlesen dieser Arbeit und die vielen interessanten und lehrreichen Diskussionen über Quantentheorie. Zu guter Letzt möchte ich noch meiner Familie für ihre Unterstützung und Geduld in dieser arbeitsintensiven Zeit danken.

Selbstständigkeitserklärung

Die vorliegende Arbeit ist von mir selbständig und nur unter Zuhilfenahme der angegebenen Quellen und Hilfsmittel angefertigt worden.

Ort,Datum	Unterschrift